大氣及幾何效應

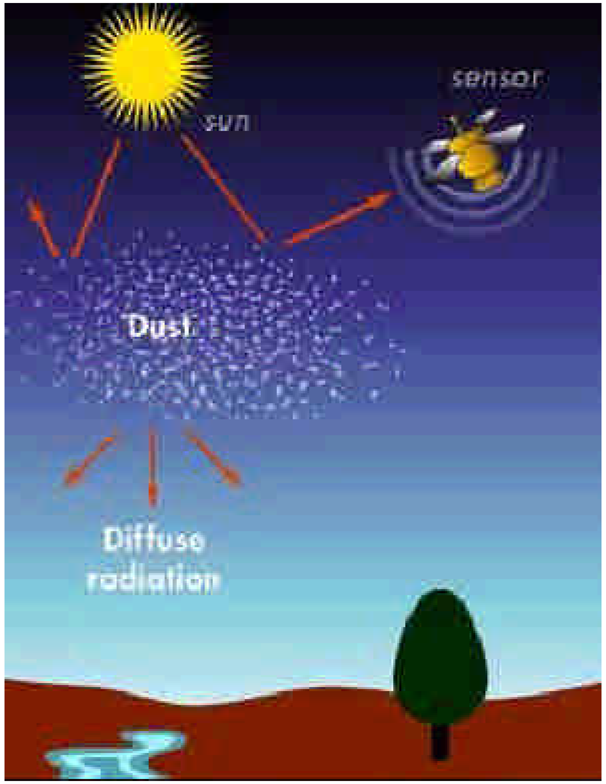
sensor
sun
Dust
Diffuse
radiation

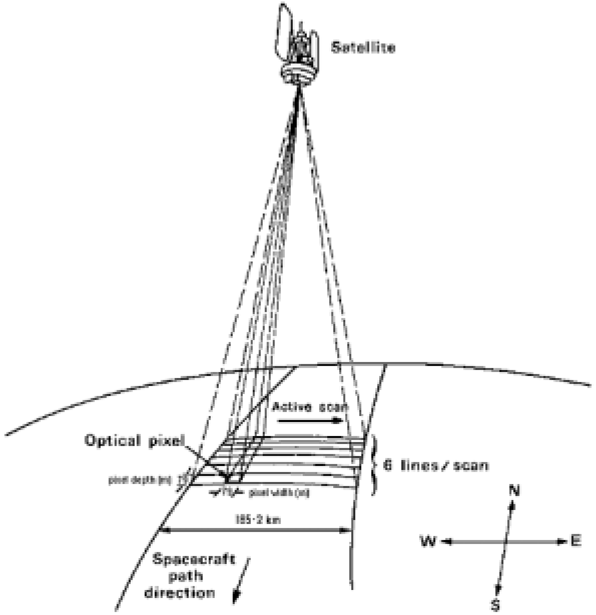
Satellite
Active scan
Optical pixel
6 lines / scan
pixel depth (m)
pixel width (m)
185·2 km
N
W
E
S
Spacecraft
path
direction

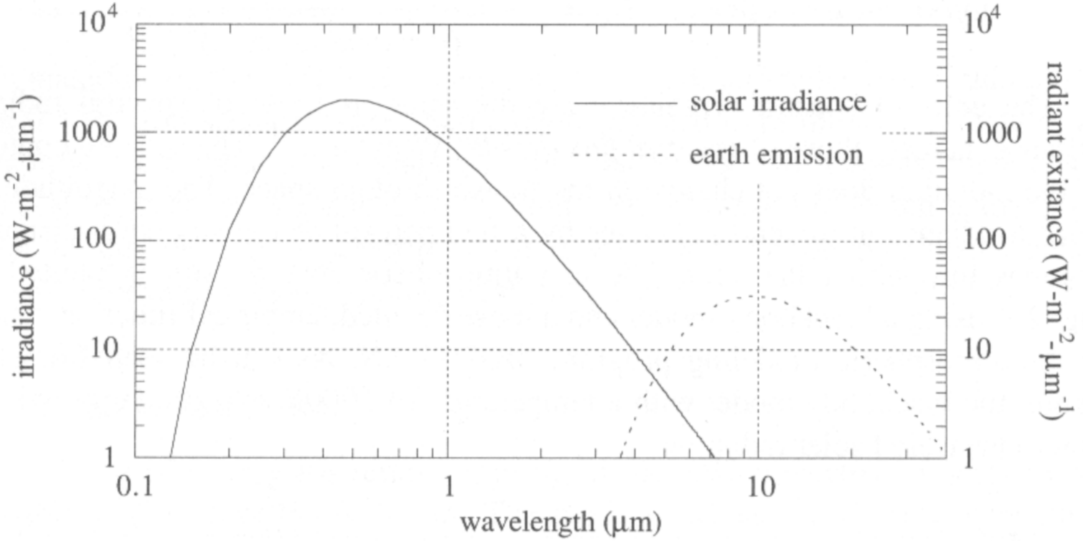

FIGURE 2-2. Spectral distributions at the top-of-the-atmosphere for the two radiation sources in the visible through thermal infrared spectral regions. The earth is assumed to be a blackbody at T = 300K and the sun a blackbody at T = 5900K, and atmospheric effects are ignored. Blackbody curves for different temperatures cannot cross each other; it only appears to occur here because the solar radiant exitance has been scaled as described in Eq. (2 – 3).

$$\text{\textit{top-of-the atmosphere:}}\quad E_\lambda^0 = \frac{M_\lambda}{\pi} \times \frac{\text{area solar disk}}{(\text{distance-to-earth})^2} \qquad (2-3)$$

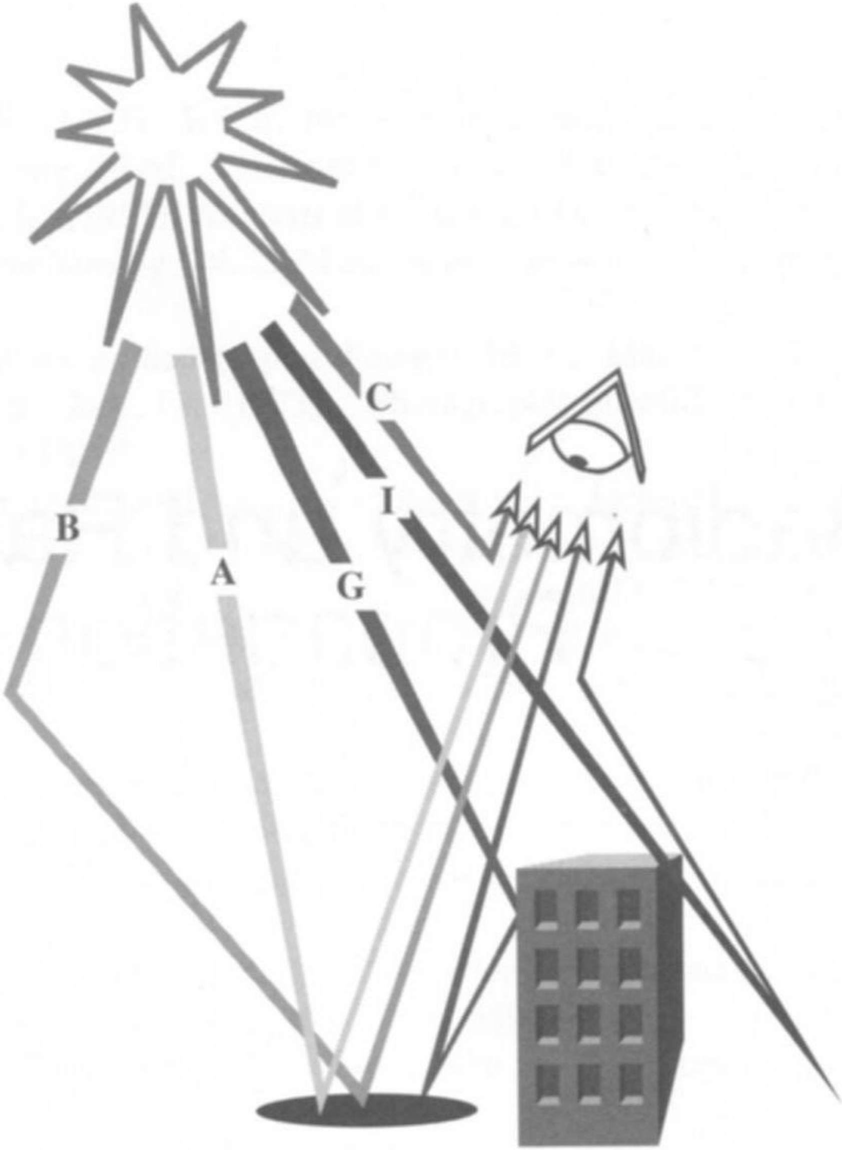

Figure 3.1 Solar energy paths.

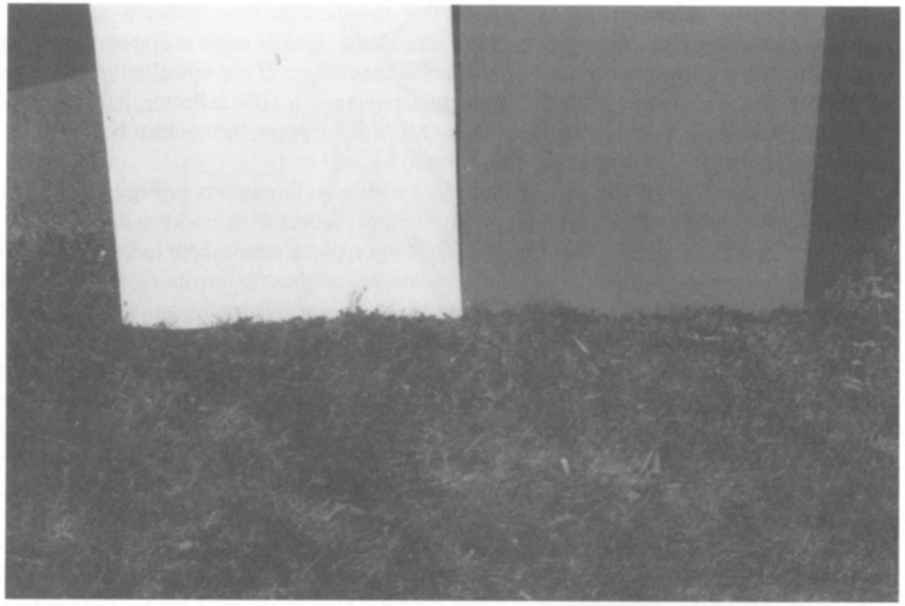

(a) Grass with black and white background.

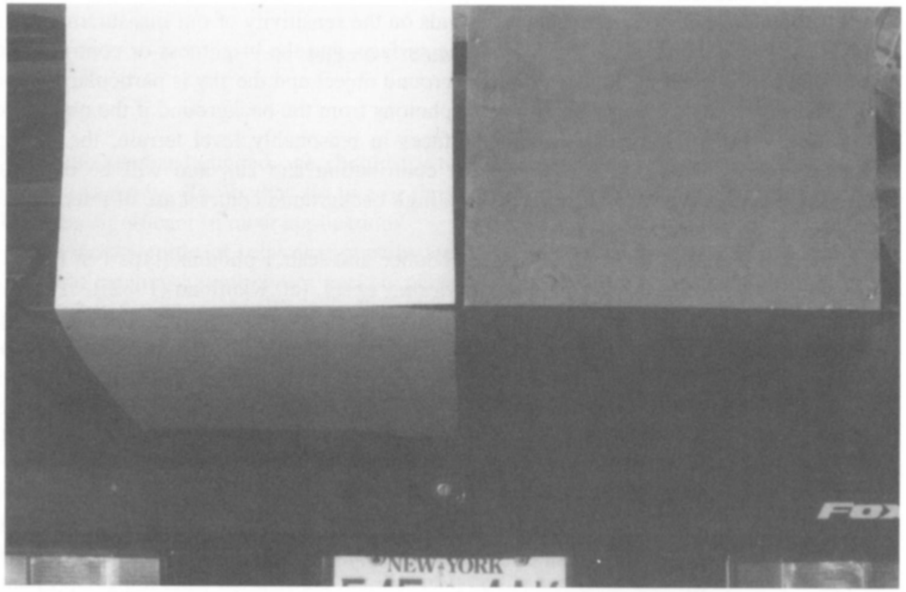

(b) Car hood with black and white background.

Figure 3.2 Illustration of multiple bounce effects.

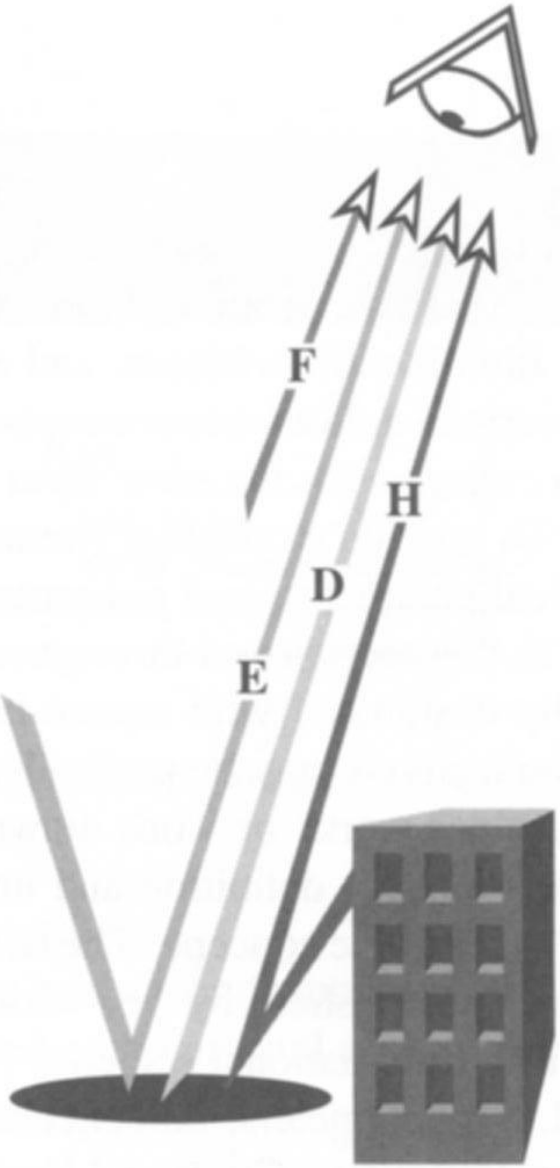

Figure 3.3 Self-emitted thermal energy paths.

$$L = L_A + L_D + L_B + L_E + L_G + L_H + L_C + L_F$$

$$L_\lambda = \{ E'_{s\lambda} \cos(\sigma)\, \tau_1(\lambda) \frac{r(\lambda)}{\pi} + \varepsilon(\lambda) L_{T\lambda} + F[E_{ds\lambda} + E_{d\varepsilon\lambda}] \frac{r_d(\lambda)}{\pi} + (1-F)[L_{bs\lambda} + L_{b\varepsilon\lambda}] r_d(\lambda) \}\, \tau_2(\lambda) + L_{us\lambda} + L_{u\varepsilon\lambda}$$

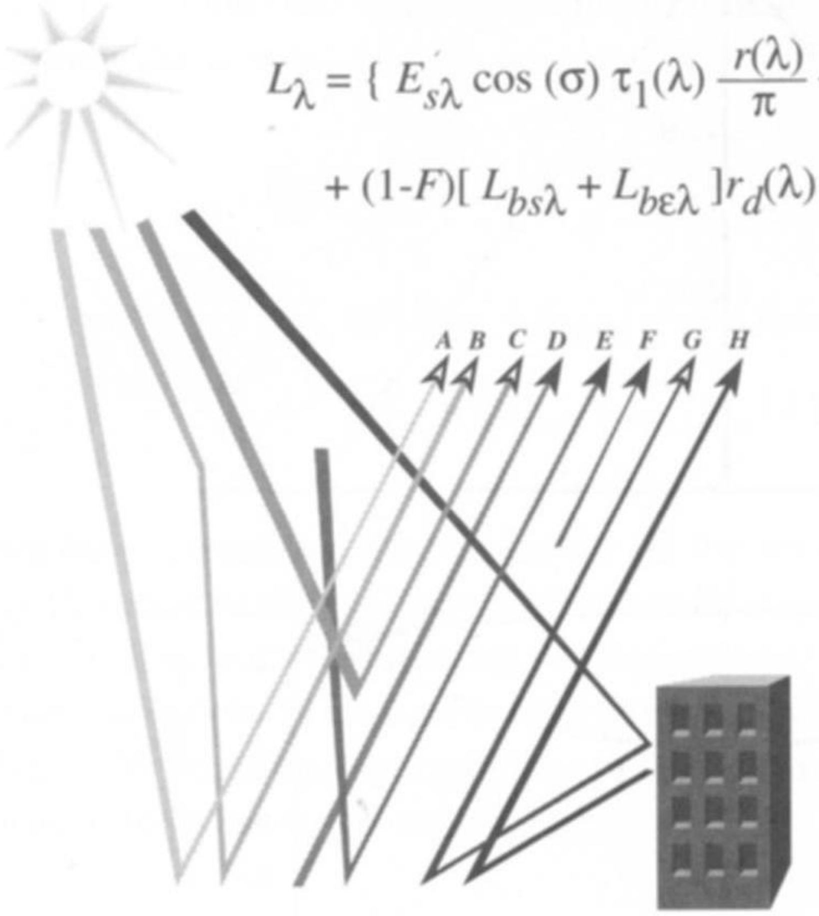

Figure 4.16 Relationship between terms in "*the big equation*" and energy paths associated with the photon flux onto the sensor.

大氣效應

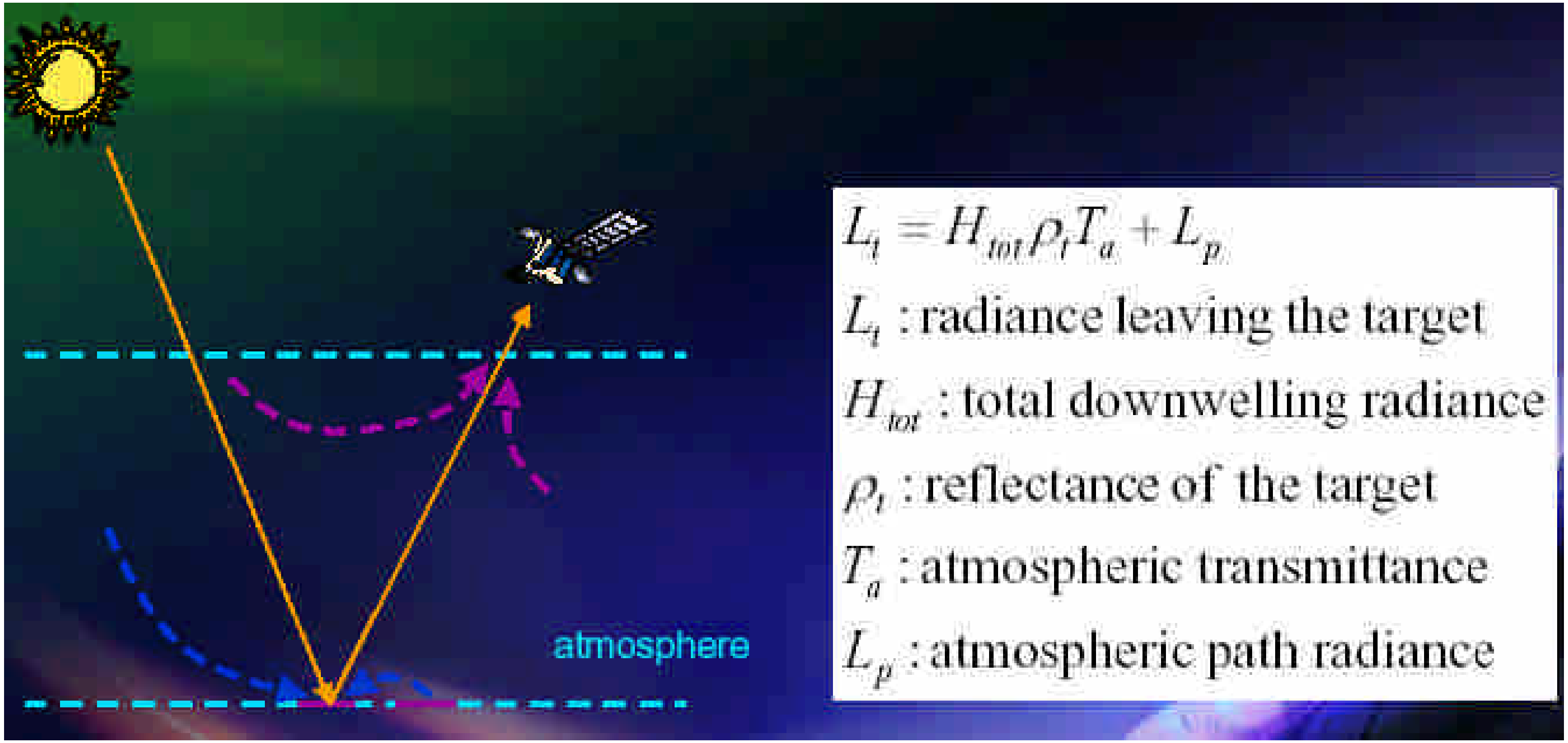

$$L_t = H_{tot} \rho_t T_a + L_p$$

L_t : radiance leaving the target

H_{tot} : total downwelling radiance

ρ_t : reflectance of the target

T_a : atmospheric transmittance

L_p : atmospheric path radiance

大氣散射

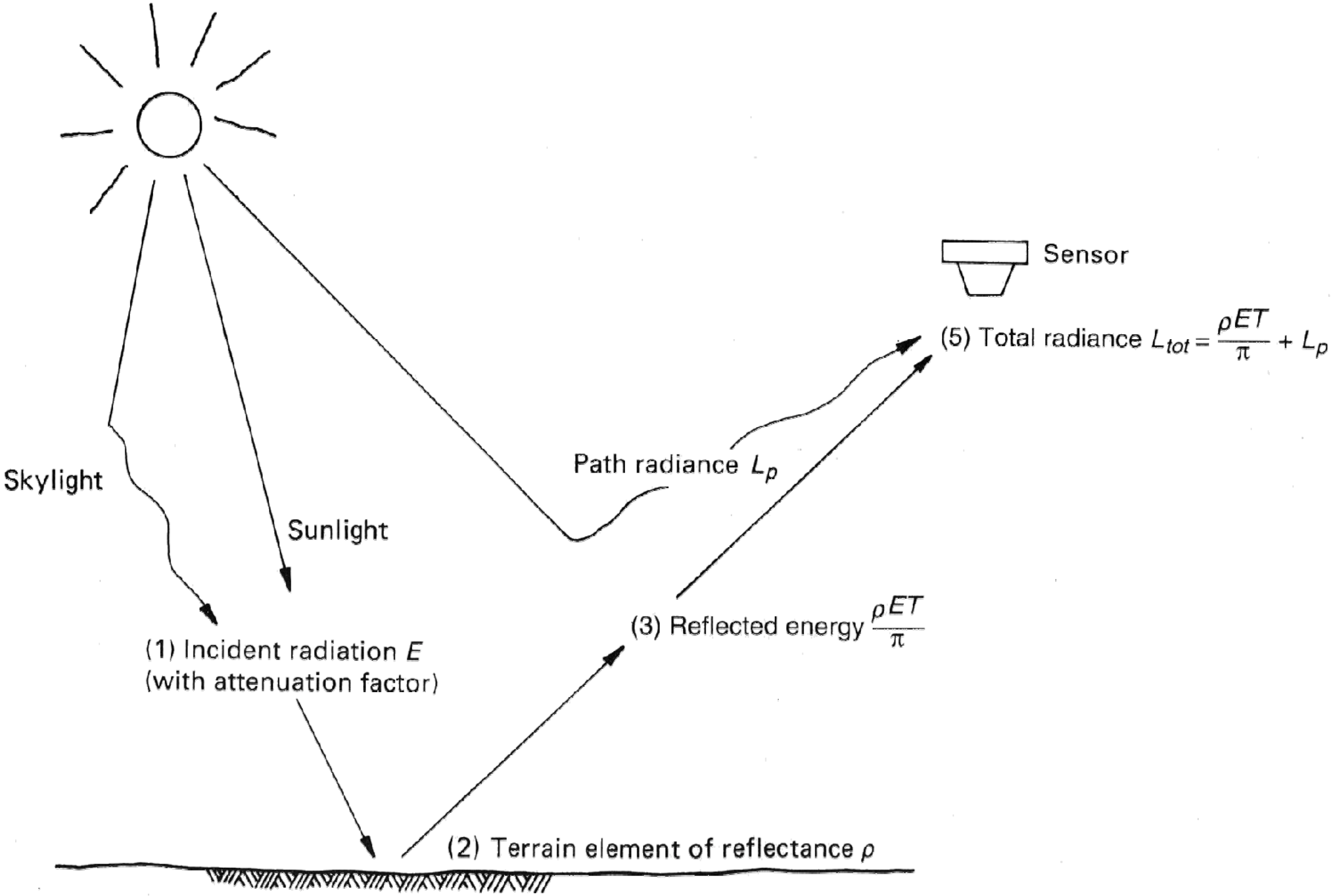
Sensor
(5) Total radiance $L_{tot} = \frac{\rho E T}{\pi} + L_p$
Path radiance L_p
Skylight
Sunlight
(3) Reflected energy $\frac{\rho E T}{\pi}$
(1) Incident radiation E
(with attenuation factor)
(2) Terrain element of reflectance ρ

大氣散射

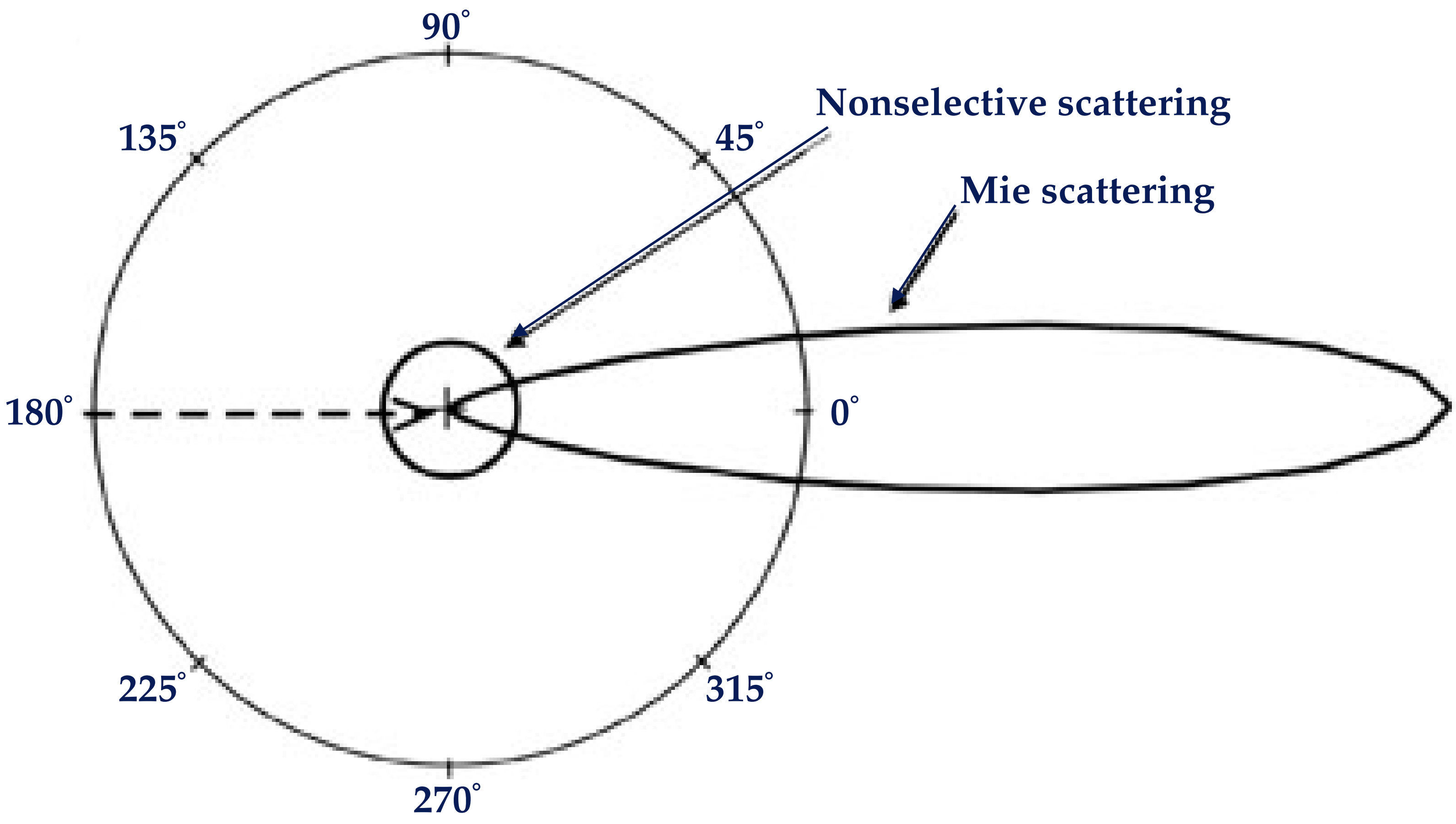
90°
Nonselective scattering
135°
45°
Mie scattering
180°
0°
225°
315°
270°

大氣散射

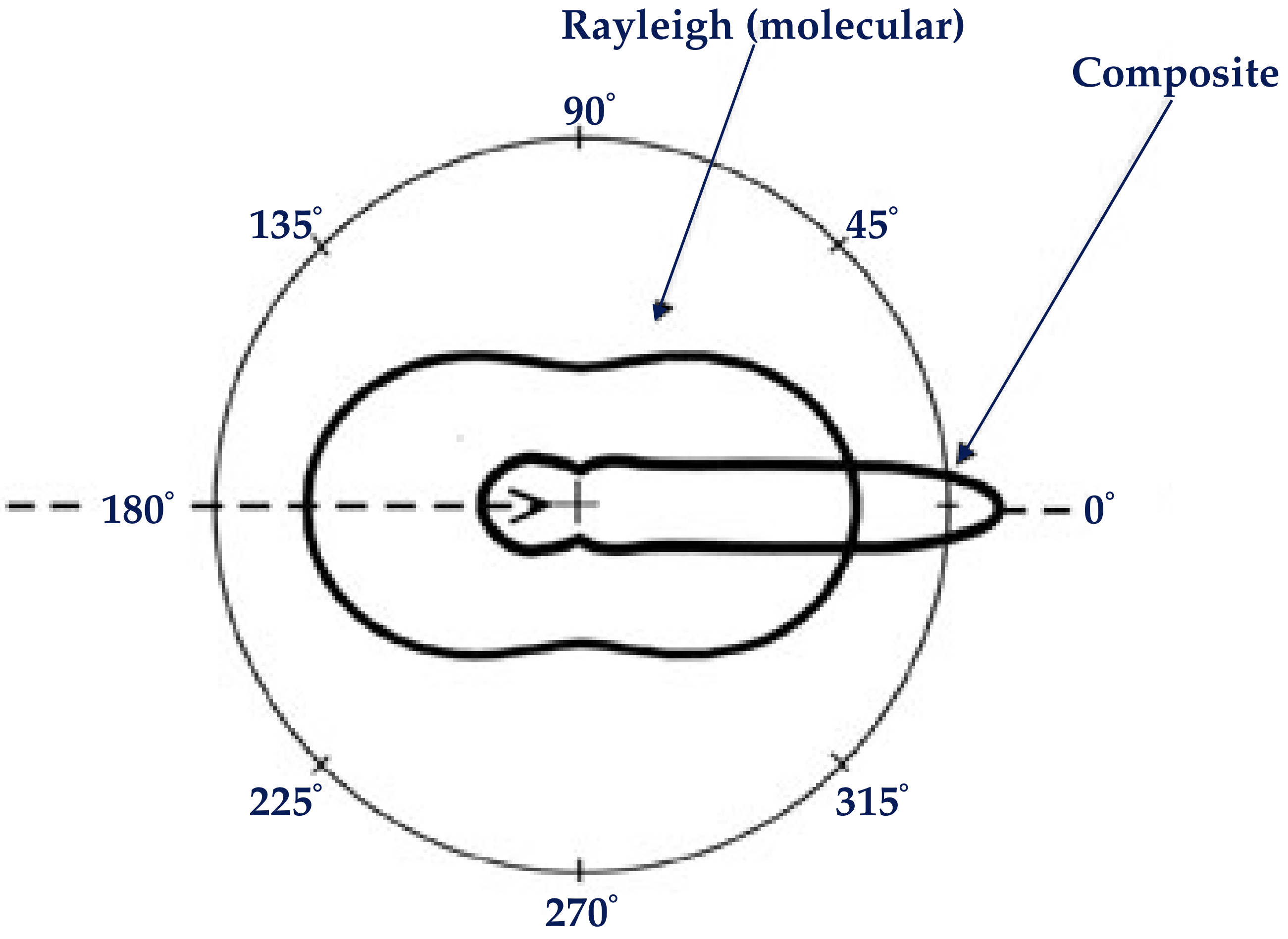

大氣吸收模式

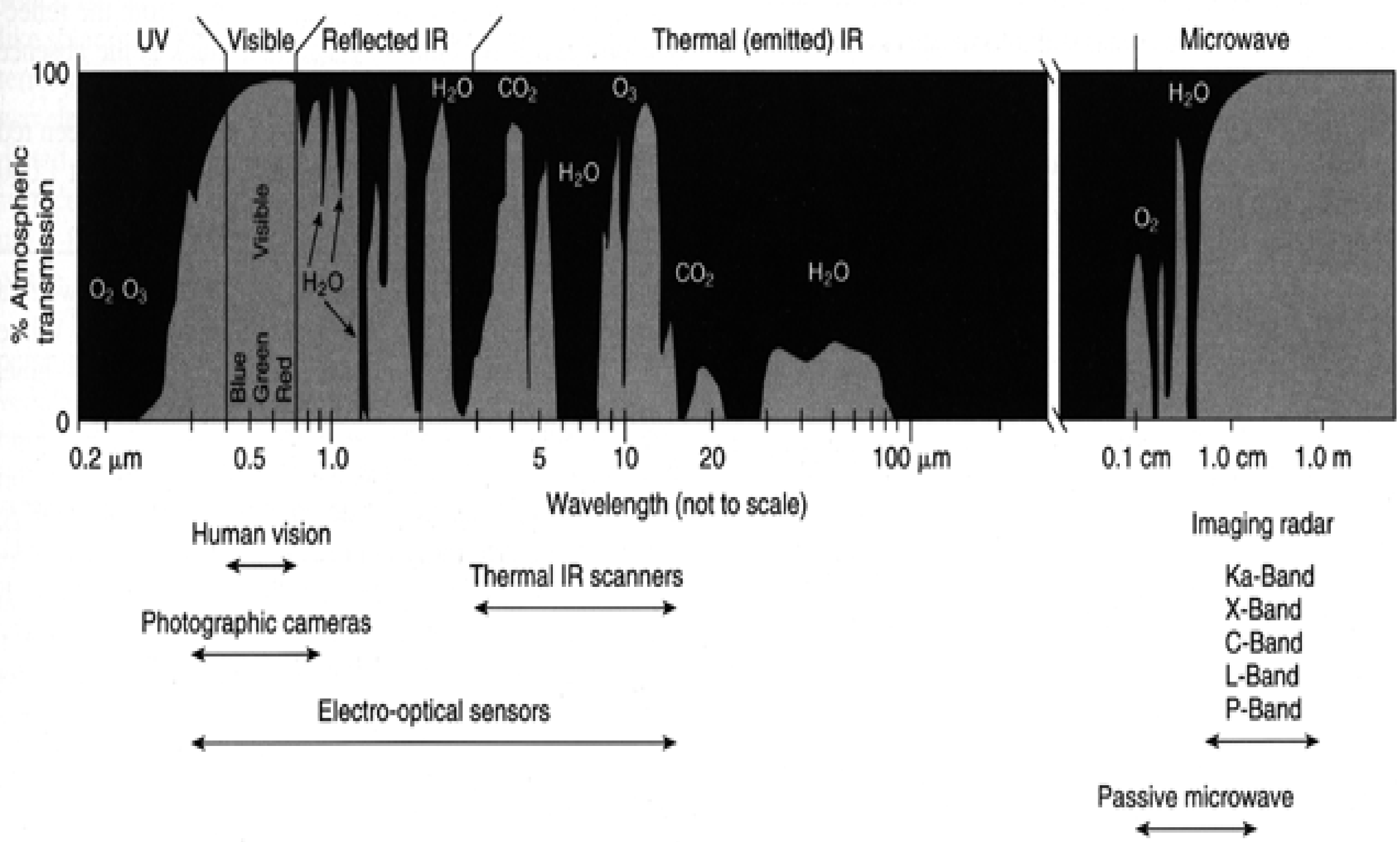
UV
Visible
Reflected IR
Thermal (emitted) IR
Microwave
100
0
% Atmospheric transmission
O_2 O_3
Visible
Blue
Green
Red
H_2O
H_2O
CO_2
O_3
H_2O
CO_2
H_2O
H_2O
O_2
0.2 µm
0.5
1.0
5
10
20
100 µm
0.1 cm
1.0 cm
1.0 m
Wavelength (not to scale)
Human vision
Photographic cameras
Electro-optical sensors
Thermal IR scanners
Imaging radar
Ka-Band
X-Band
C-Band
L-Band
P-Band
Passive microwave

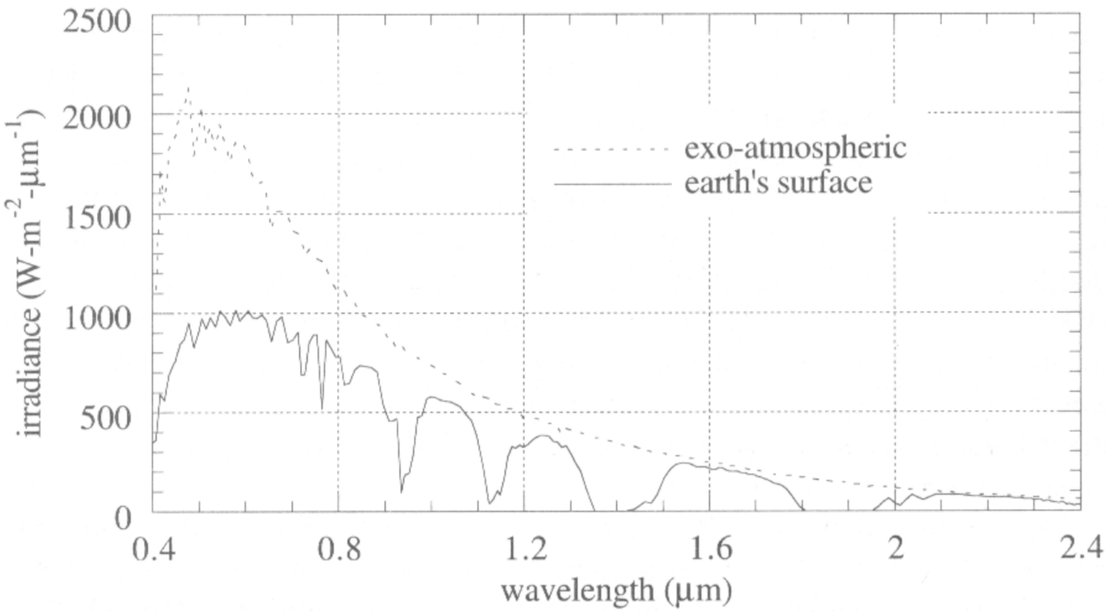

FIGURE 2-5. Solar irradiance in the visible and shortwave IR regions (for a solar elevation angle of 45°), above the atmosphere and at the earth's surface. The ratio of these two curves is the path transmittance depicted in Fig. 2-4.

大氣校正

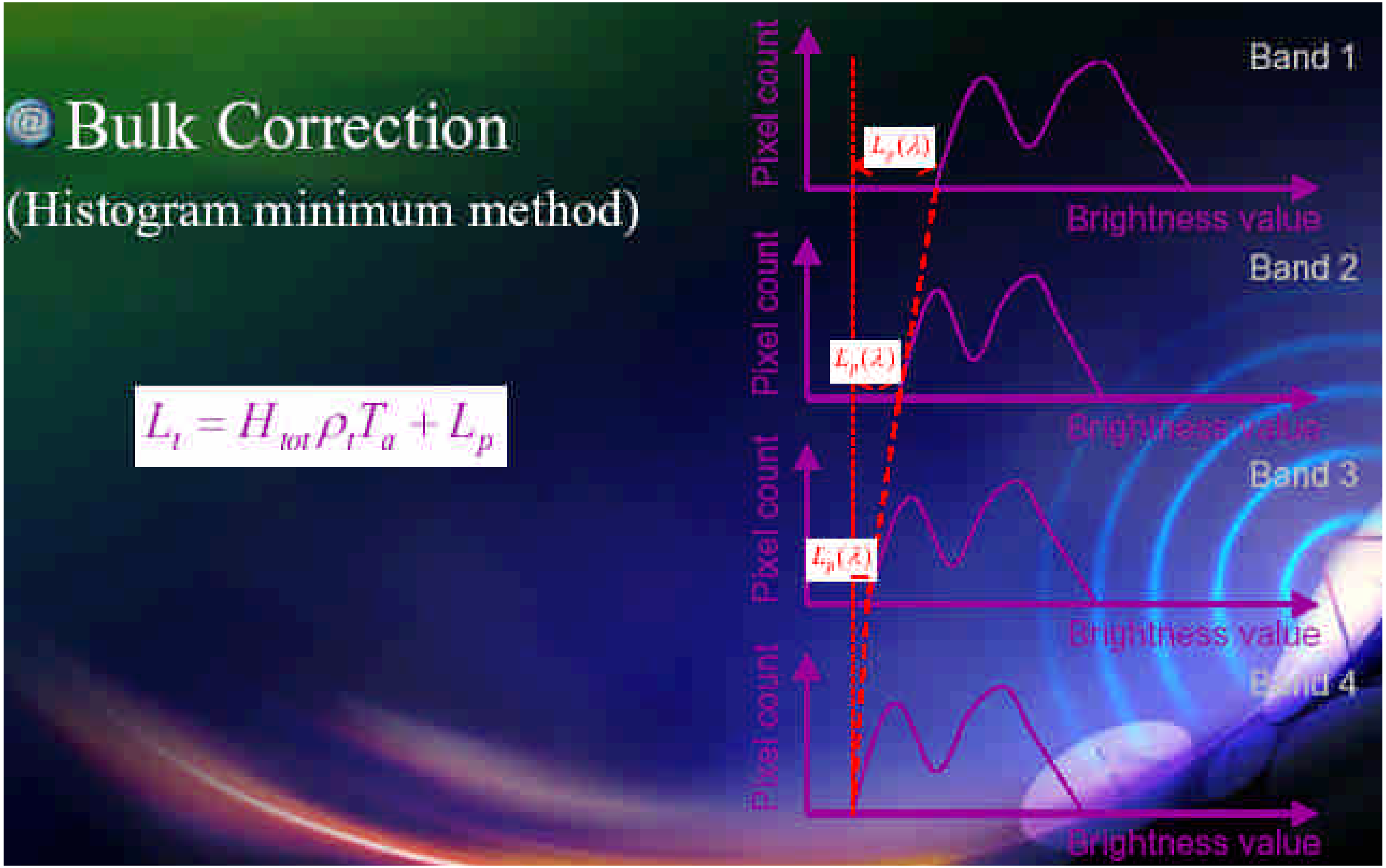

Bulk Correction

(Histogram minimum method)

$$L_t = H_{tot}\rho_t T_a + L_p$$

大氣校正

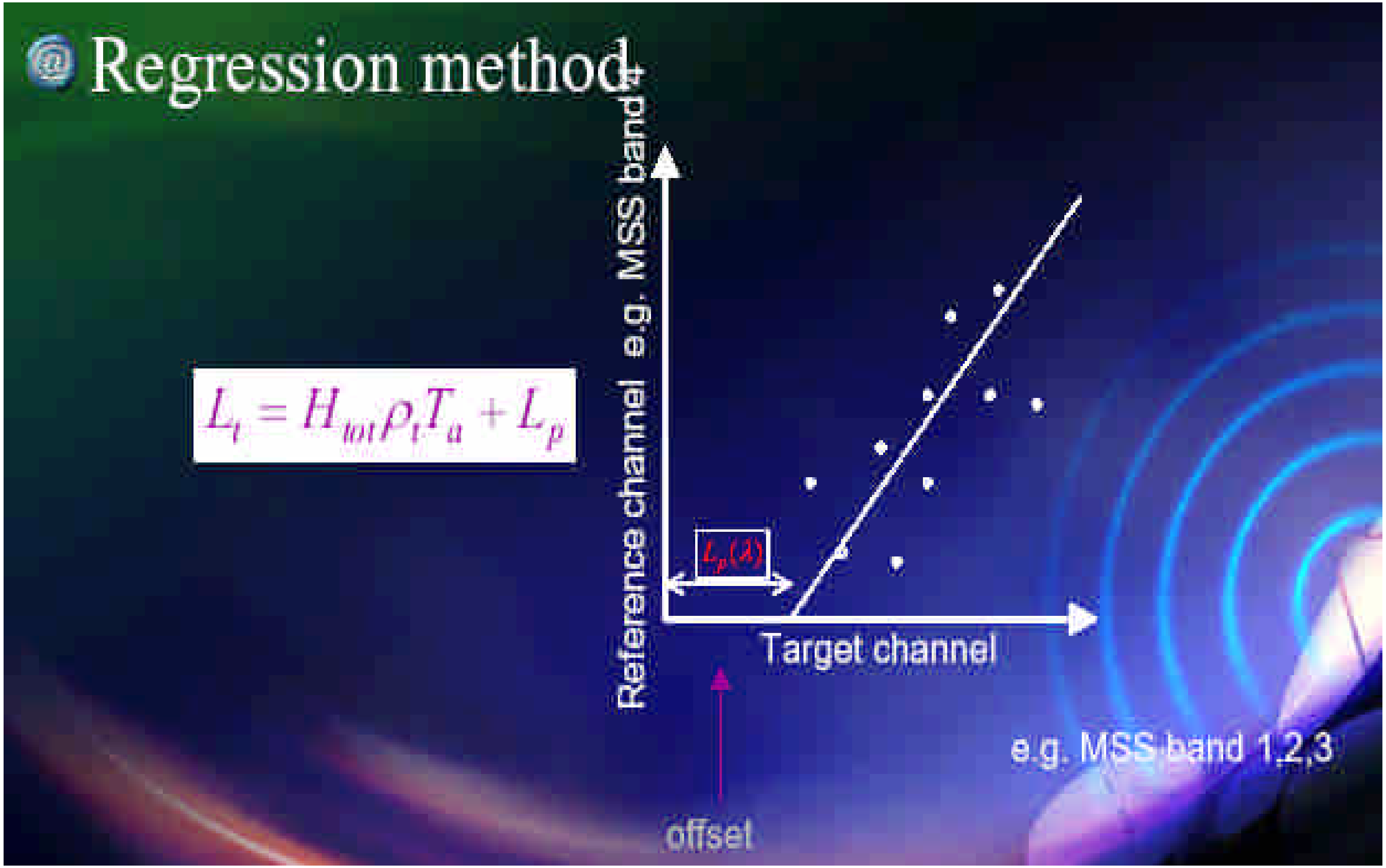

Regression method

$$L_t = H_{tot}\rho_t T_a + L_p$$

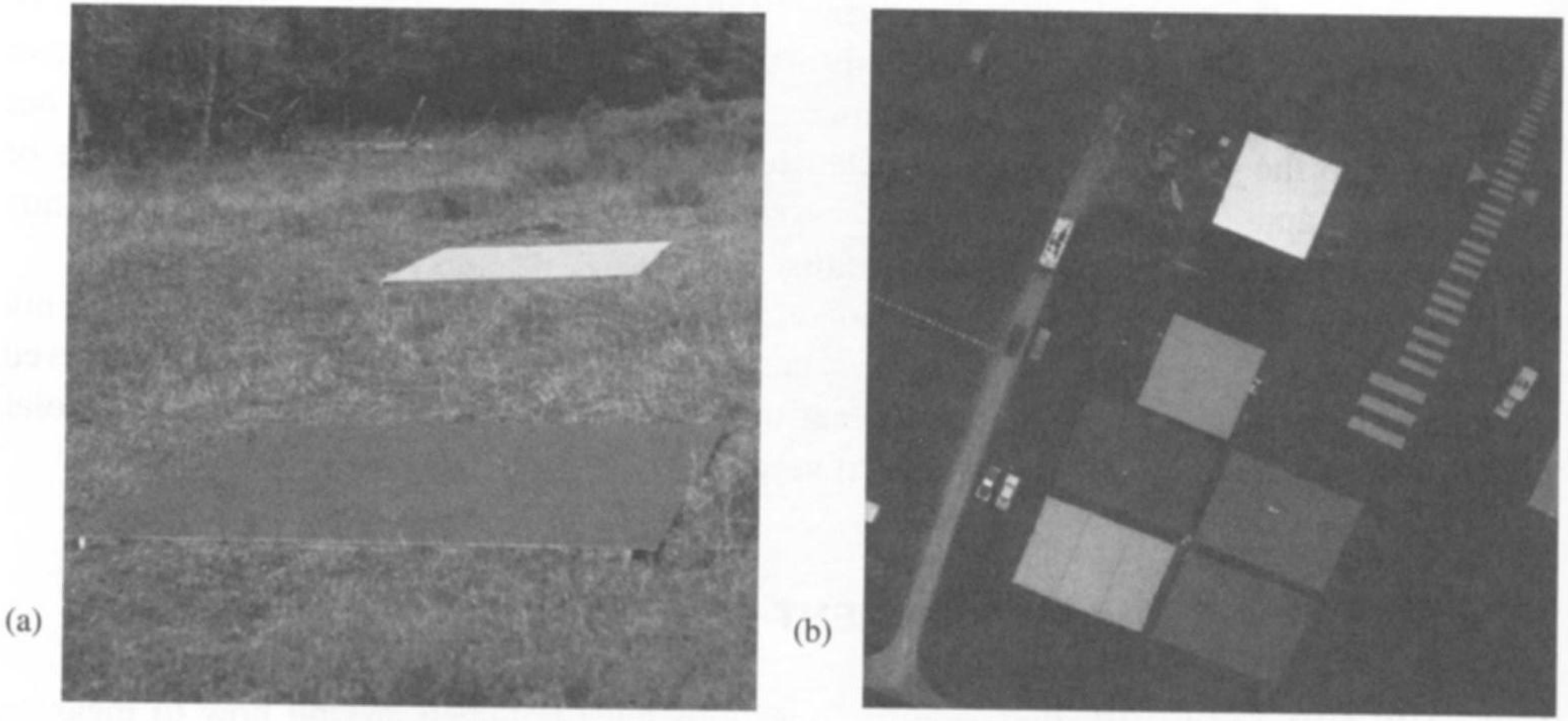

Figure 6.10 Ground control panels used for atmospheric calibration. (a) Control panels, (b) Image of control panels.

Figure 6.11 The reflectomobile used by Slater et al., 1987, in calibration of satellite sensors. The radiometers are calibrated in the field with reflectance standards and then driven over a study site to generate mean reflectance over a large, approximately uniform surface. (Courtesy of Phil Slater, University of Arizona.)

幾何誤差之原因

- 儀器誤差
  - 光學系統之變形
  - 非線性掃描
  - 非等距取值
- 全景之變形
  - 感應器的 angular FOV 不同
- 地球自轉
- 地表曲率
- 載具不穩定

Sources of Geometric Error

- Earth Rotation Effect

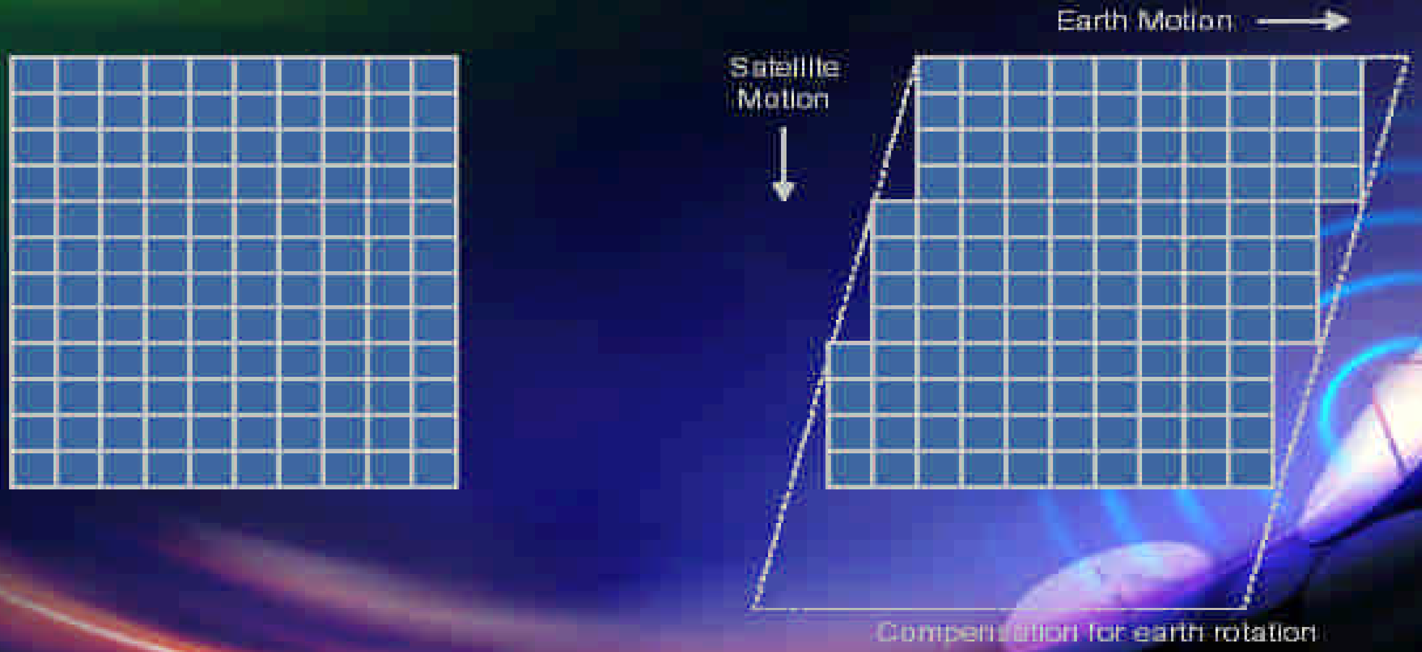

載具不穩定

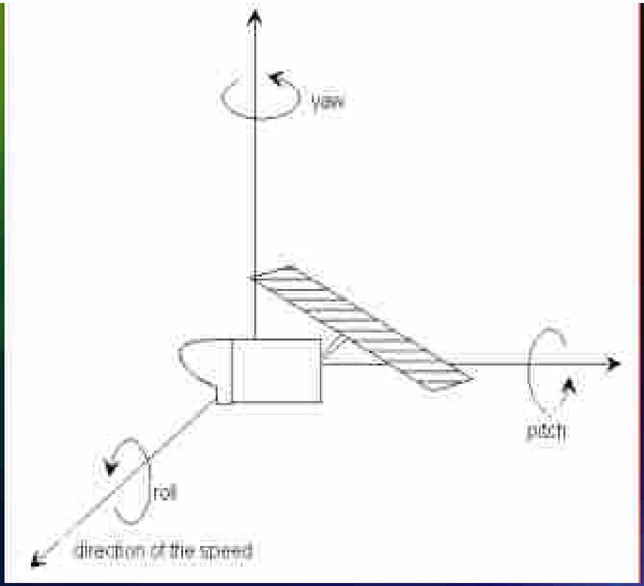

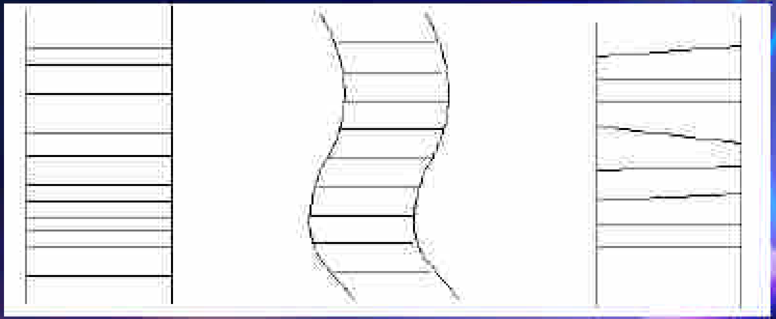

Pitch **Roll** **Yaw**

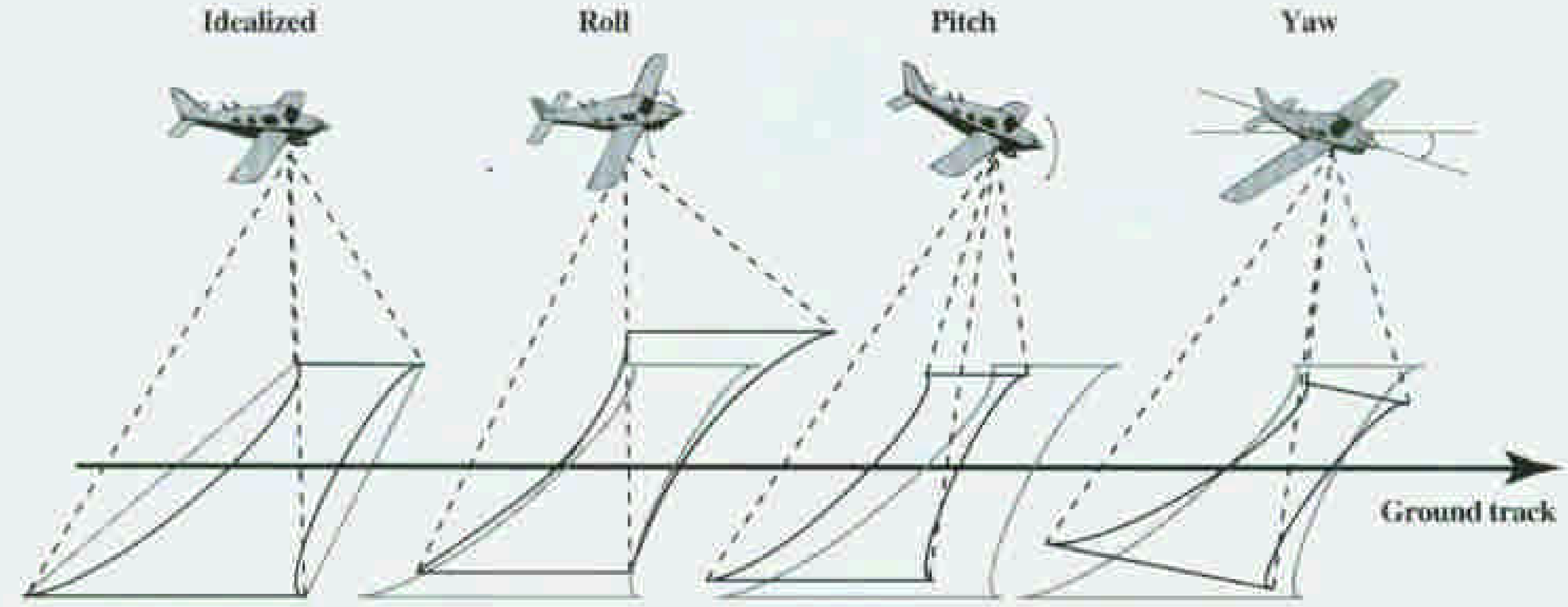

Figure 5.17 Geometric distortions due to aircraft orientation. Gray boundries represent nominal coverage; black boundries represent actual coverage.


(a)

(b)

Figure 5.18 Portion of a thermal infrared (8 to 14 μm) line scanner image: (a) before and (b) after lines were shifted to correct for roll distortion. (Image courtesy of the Rochester Institue of Technology, DIRS Lab.)

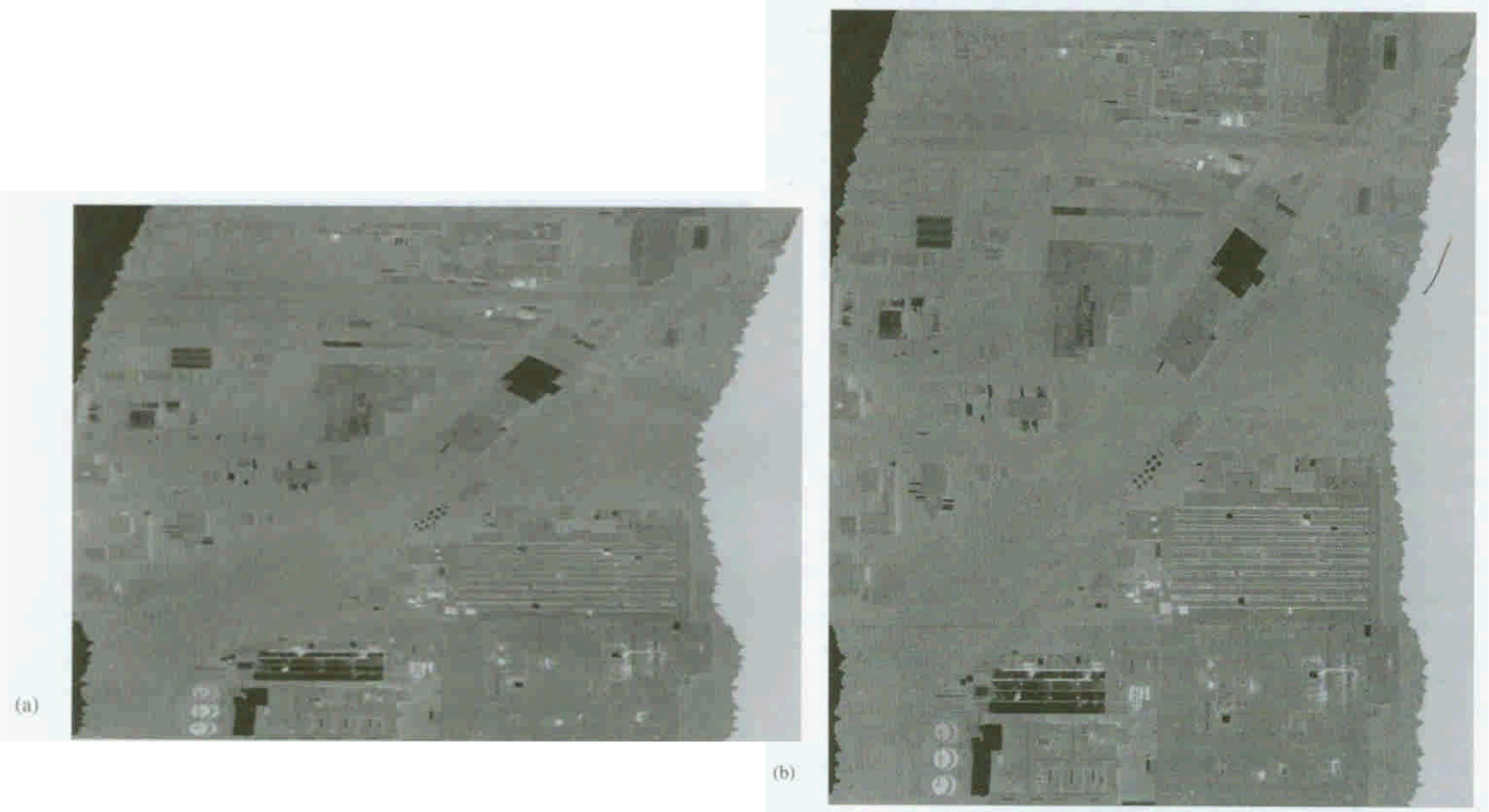

Figure 5.19 Thermal infrared image showing V/H distortion: (a) original image, (b) after resampling to proper V/H ratio. (Imagery courtesy of the Rochester Institute of Technology, DIRS Lab.)

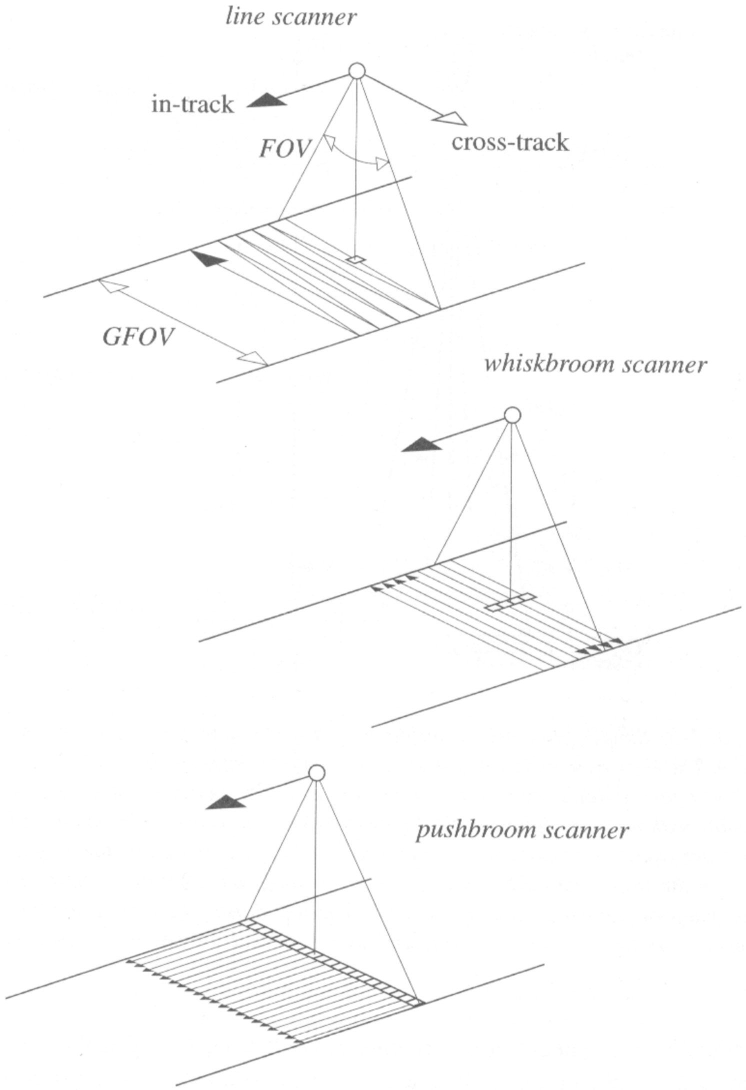

FIGURE 1-8. Definition of basic scanner parameters and depiction of three types of scanning methods. The solid arrows represent motion relative to a stationary earth. In reality, the earth is rotating during the scanning process, approximately in the cross-track direction since most satellite remote-sensing systems are in a near-polar orbit. This results in a east-west skew in the surface coverage over the full scene.

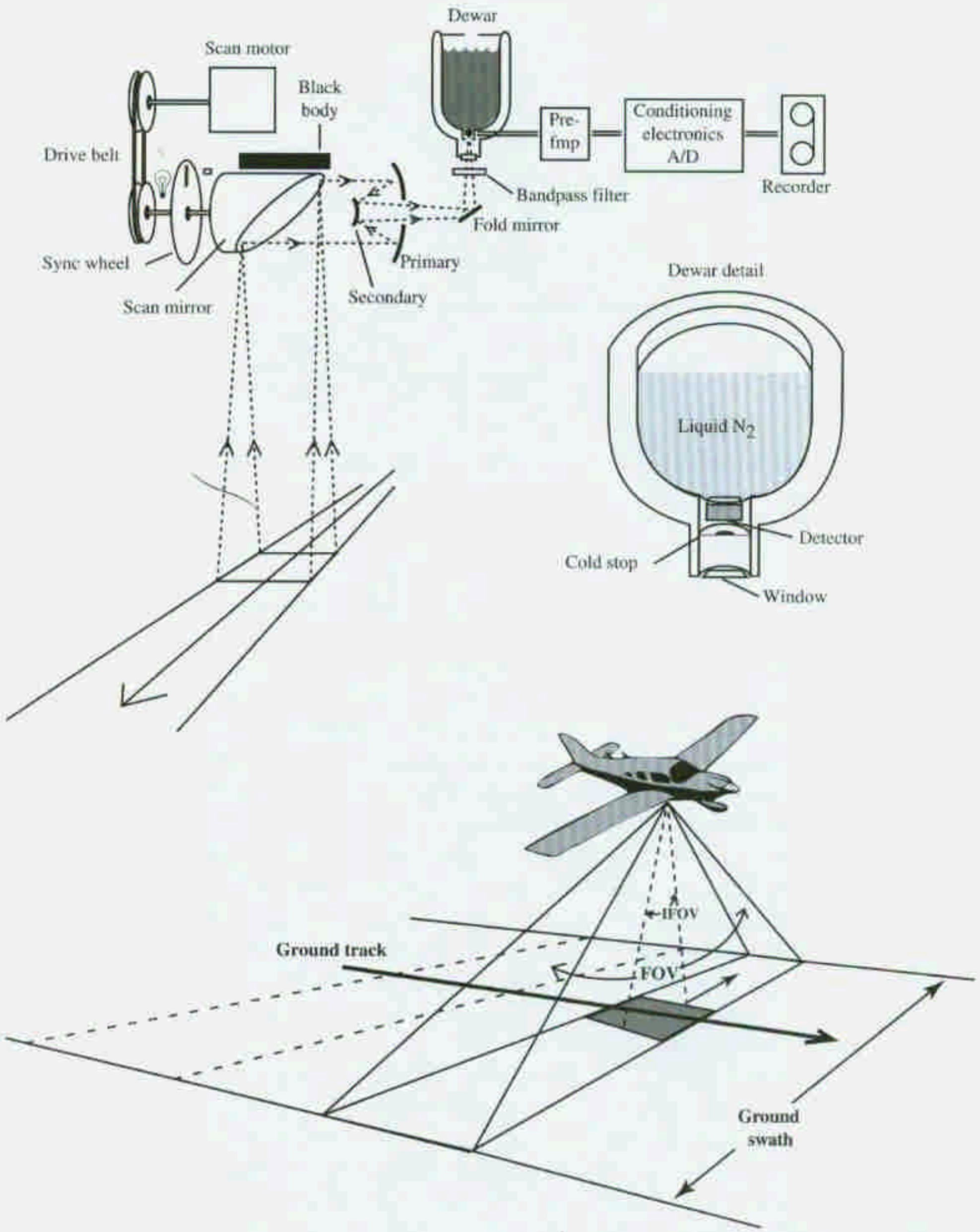

Figure 5.16 Line scanner design and collection scheme. A thermal infrared line scanner is shown with liquid nitrogen cooling of the detector and coldstop.

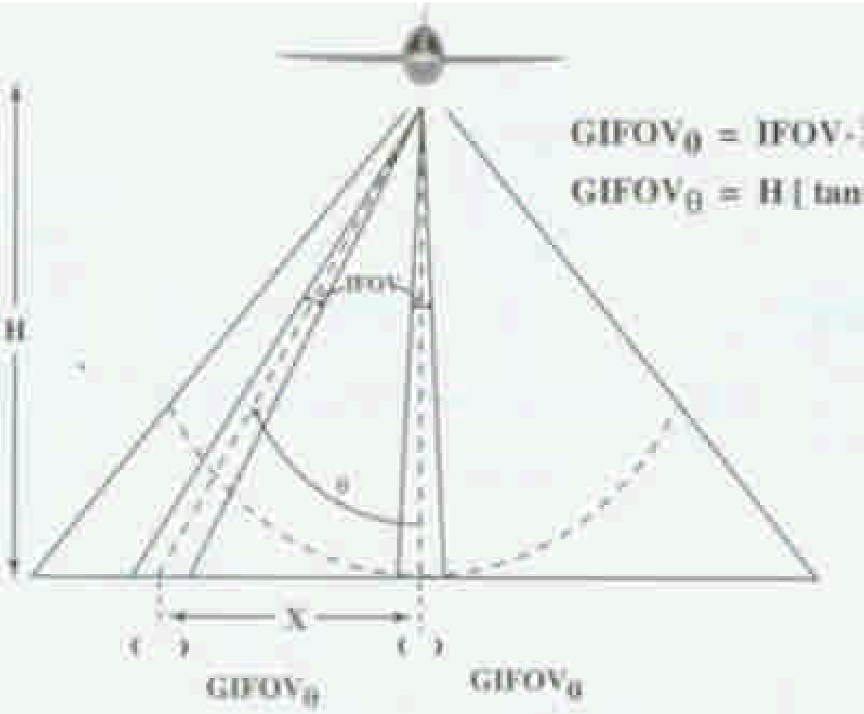

$$GIFOV_\theta = IFOV \cdot H$$

$$GIFOV_\theta = H\left[\tan\left(\theta + \frac{IFOV}{2}\right) - \tan\left(\theta - \frac{IFOV}{2}\right)\right]$$

Figure 5.20 Tangent error effects. The diagonal roads in the thermal infrared line scanner image should be straight, and the tanks in the lower left roughly corcular. (a) Original image, (b) image after tangent correction. (Image courtesy of the Rochester Institute of Technology, DIRS lab.)

$$\textit{flat earth:}\quad GSI_f(\theta)/GSI(0) = [1/\cos(\theta)]^2 \quad , \qquad (3-29)$$

$$\textit{spherical earth:}\quad GSI_e(\theta)/GSI(0) = \frac{[H + r_e(1-\cos\phi)]}{H\cos(\theta)\cos(\theta+\phi)} \qquad (3-30)$$

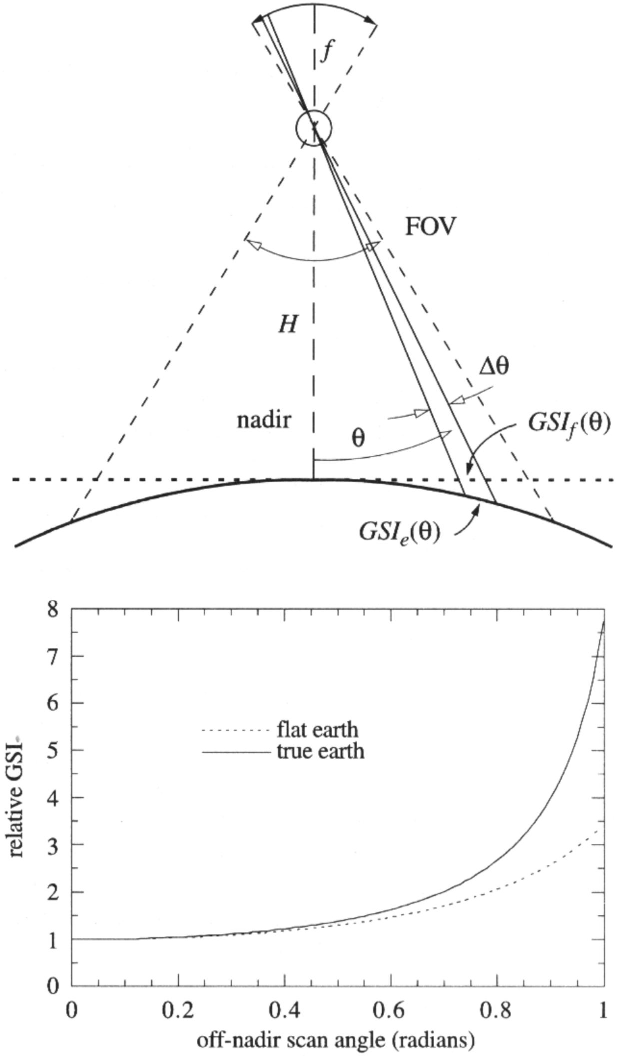

FIGURE 3-22. Line and whiskbroom scanner geometry in the cross-track direction, used to derive Eq. (3 – 29) and Eq. (3 – 30). The data along the scan is sampled at a fixed time interval to create pixels. Assuming the scan rotational velocity is constant, that interval corresponds to a fixed angular interval, Δθ. The cross-track GSI therefore increases with increasing θ, as shown below for an altitude of 850km. The flat earth approximation is good within 4% out to a scan angle of about 0.4 radians, or 23°.

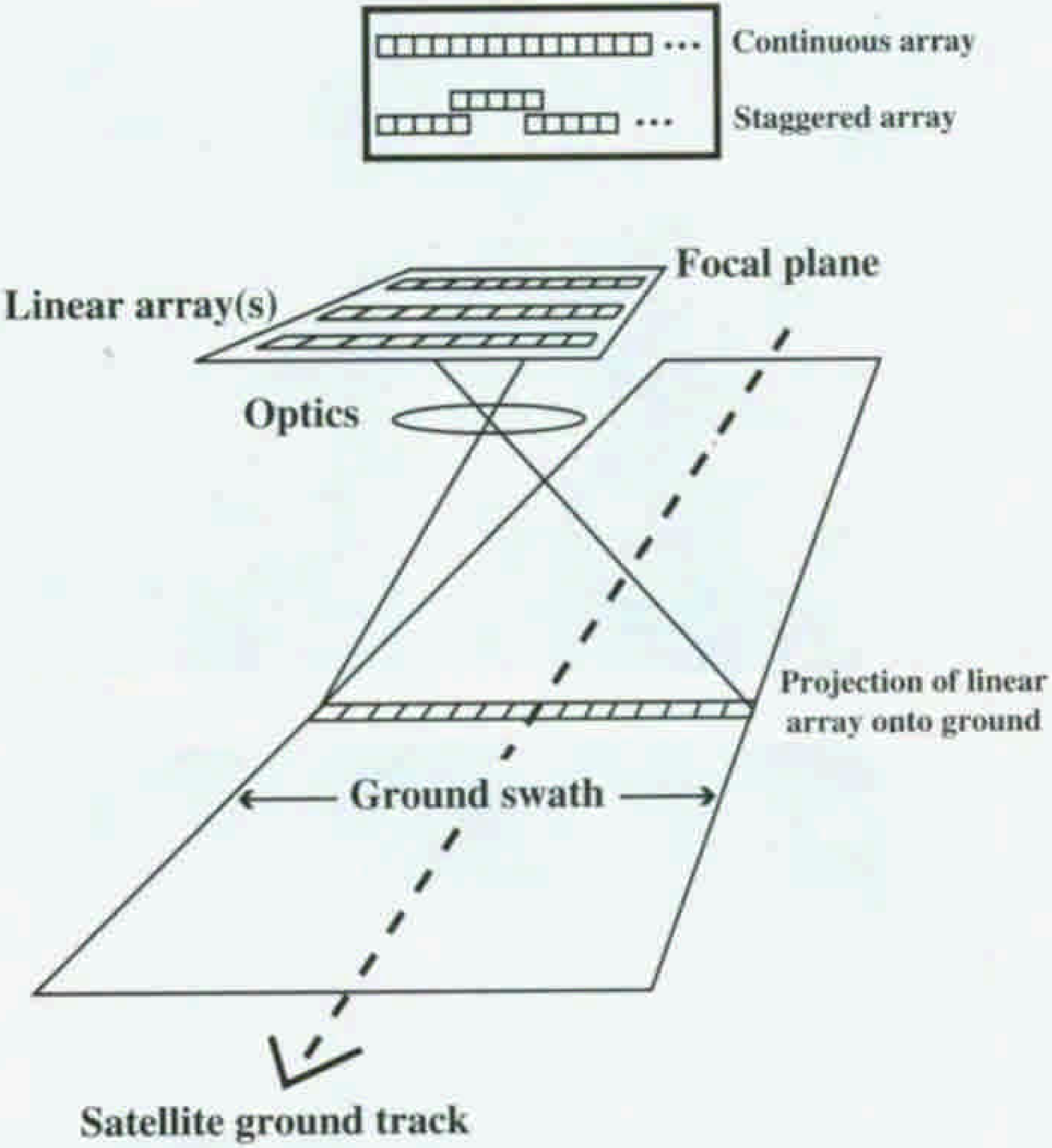

Figure 5.29 Push-broom sensor operation.

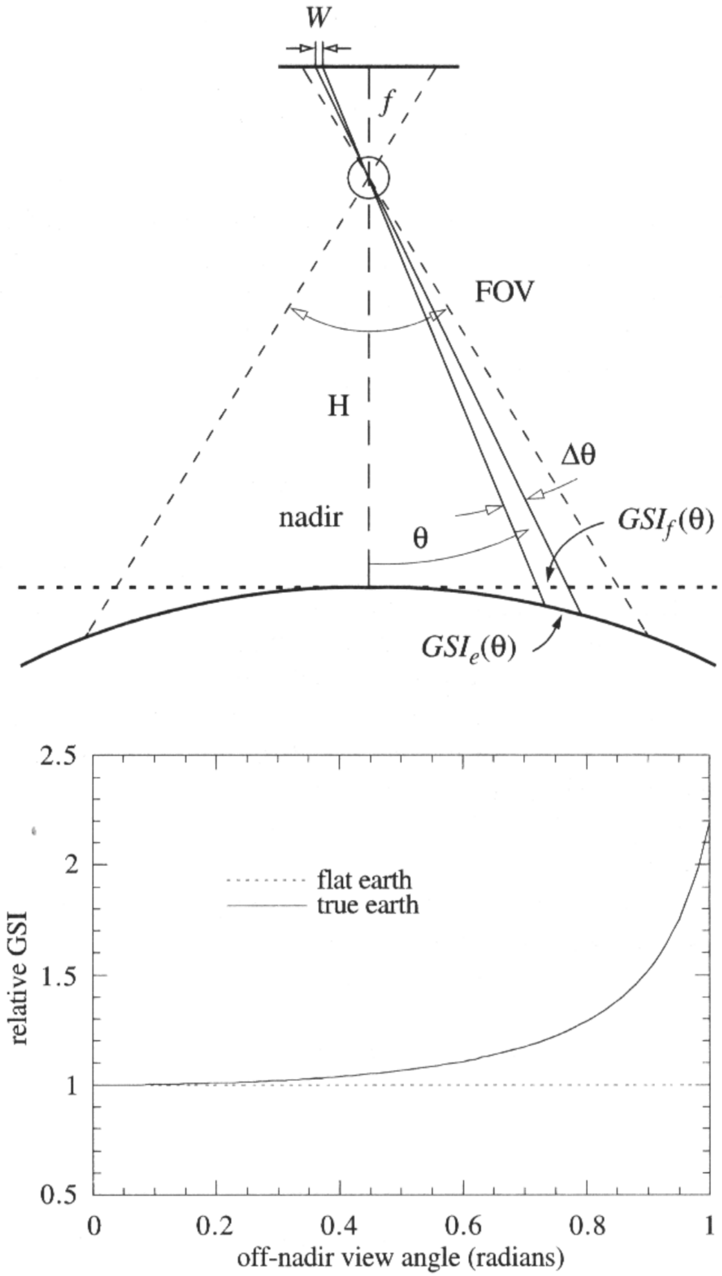

$$\text{flat earth:} \quad GSI_f = w \times \frac{H}{f}, \qquad (3-32)$$

$$\text{spherical earth:} \quad GSI_e(\theta)/GSI(0) = \frac{[H + r_e(1-\cos\phi)]\cos(\theta)}{H\cos(\theta+\phi)} \qquad (3-34)$$

FIGURE 3-24. Cross-track pushbroom scanner geometry for Eq. (3 – 32) and Eq. (3 – 34). The cross-track GSI is constant under the flat earth approximation, but increases with increasing view angle θ for the true spherical earth. The altitude used is 832km, corresponding to the SPOT satellites.

幾何校正

- 與地圖對應
- 控制點對應
- 用鄰近影像校正
- 與同地區不同時間影像對應
- 與同地區不同感應器影像對應
- 應用地理資訊系統

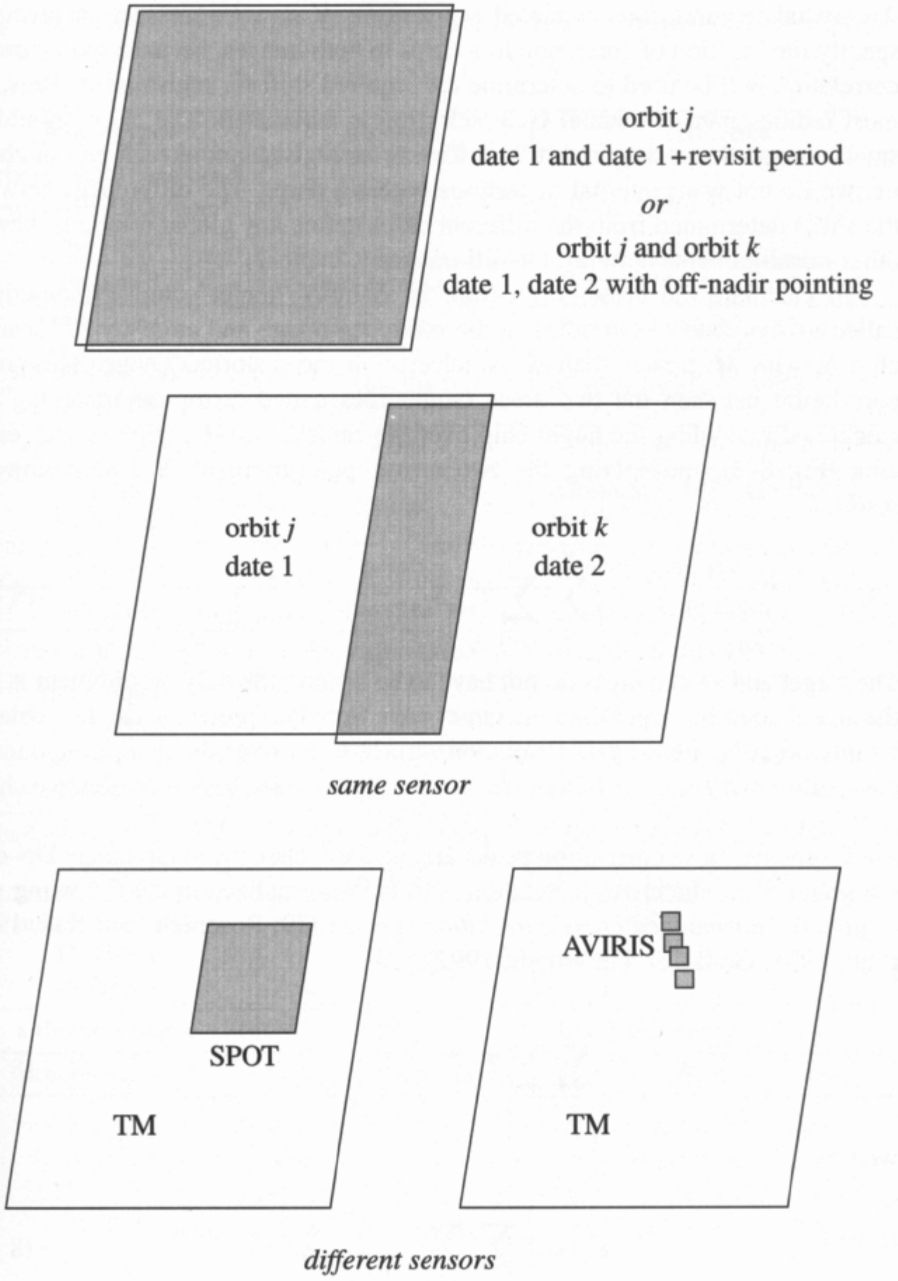

FIGURE 8-1. Ways to obtain multitemporal data of the same area from a single satellite sensor or two different sensors. The ground coverage of the images is shown.

Geometric processing data flow

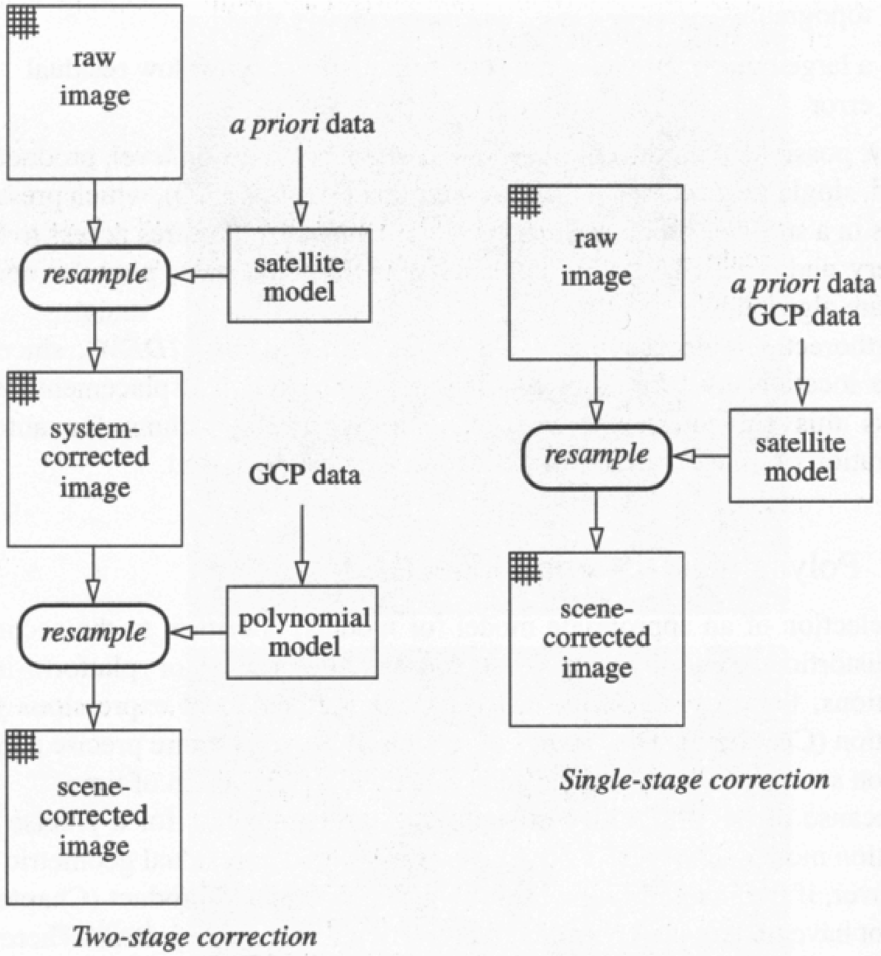

FIGURE 7-29. Geometric processing data flow for the common two-stage process and a single-stage process for rectification. In the two-stage process, a generic polynomial model is used to remove residual distortions in the system-corrected imagery. The polynomial correction approach is widely used and available in all major software systems. A more sophisticated and efficient approach is to use physical models and include all corrections in a single resampling. (Adapted from (Westin, 1990).)

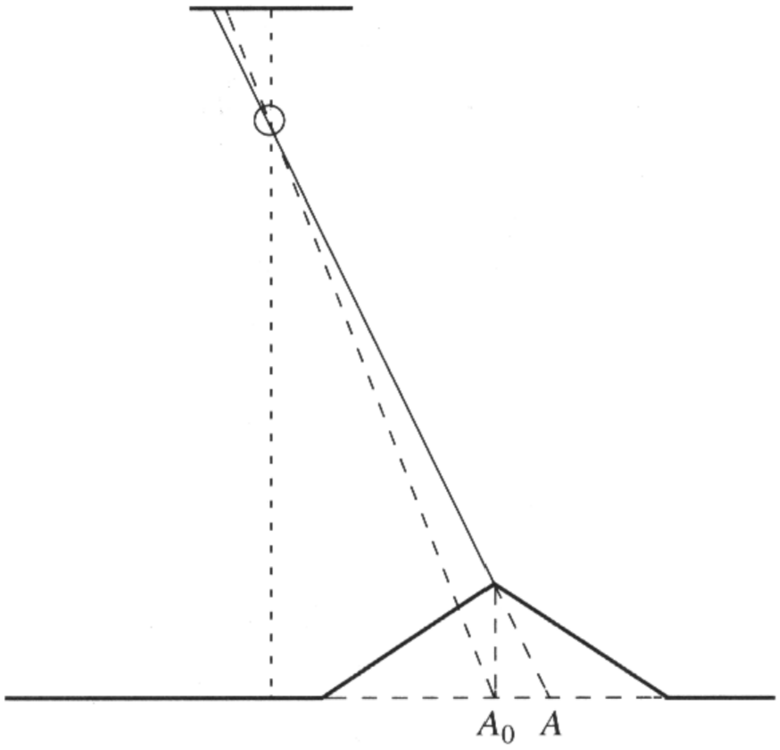

FIGURE 3-25. Geometry for a pushbroom scanner imaging a topographic feature off-nadir in the cross-track direction. The in-track vector is pointing out of the page. The image of the peak appears to come from A because of optical parallax. If the image were orthographic, the image of the peak would appear to come from A_0.

FIGURE 8-5. The full frame as scanned from a National Aerial Photography Program (NAPP) aerial photograph of Harrisburg, Pennsylvania, acquired on April 8, 1993. The eight marks around the border are the camera fiducial marks, exposed onto every frame and used to orient the internal camera model that relates the scan coordinates to the camera coordinates. This is necessary because the scan may not be exactly orthogonal to the camera frame. (The image and DEM data in this example are courtesy of George Lee and Brian Bennett of the U.S. Geological Survey, Western Mapping Center.)

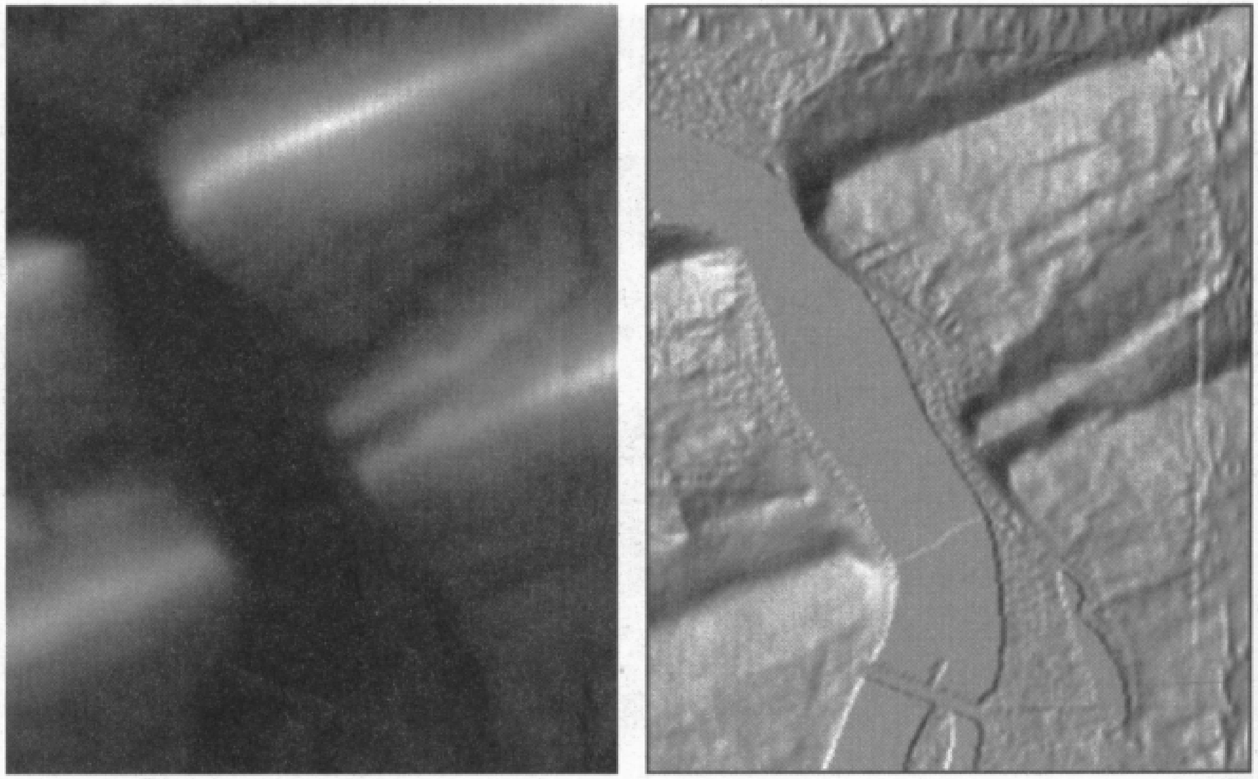

FIGURE 8-6. The Harrisburg NE quarter quad DEM (left) and a shaded relief representation (right). As we have seen before, the shaded relief image is similar to the remote-sensing image (compare to Fig. 8-5).

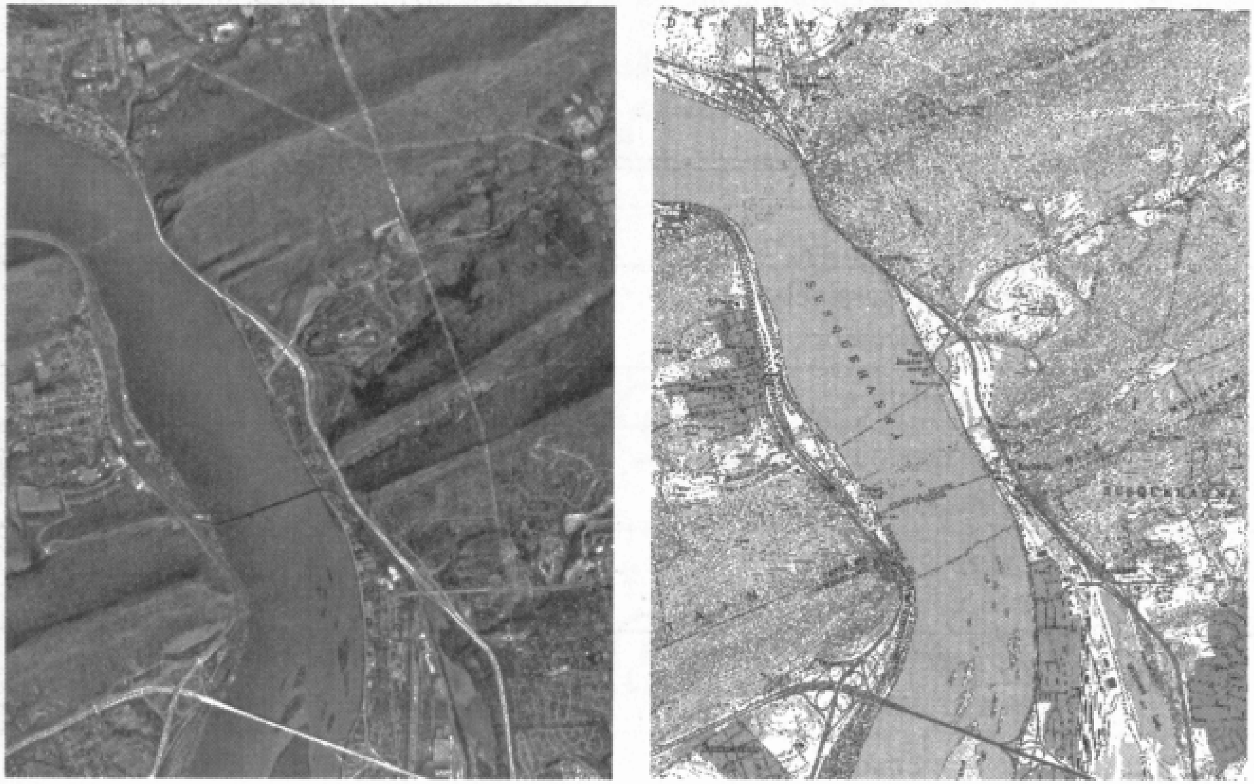

FIGURE 8-7. The digital orthophoto (left) and the corresponding portion of the quadrangle map (right). Note the precise alignment, independent of elevation. The topographic map image was scanned and resampled to a 2.4m GSI from the original 1:24,000 scale paper map (USGS, 1995).

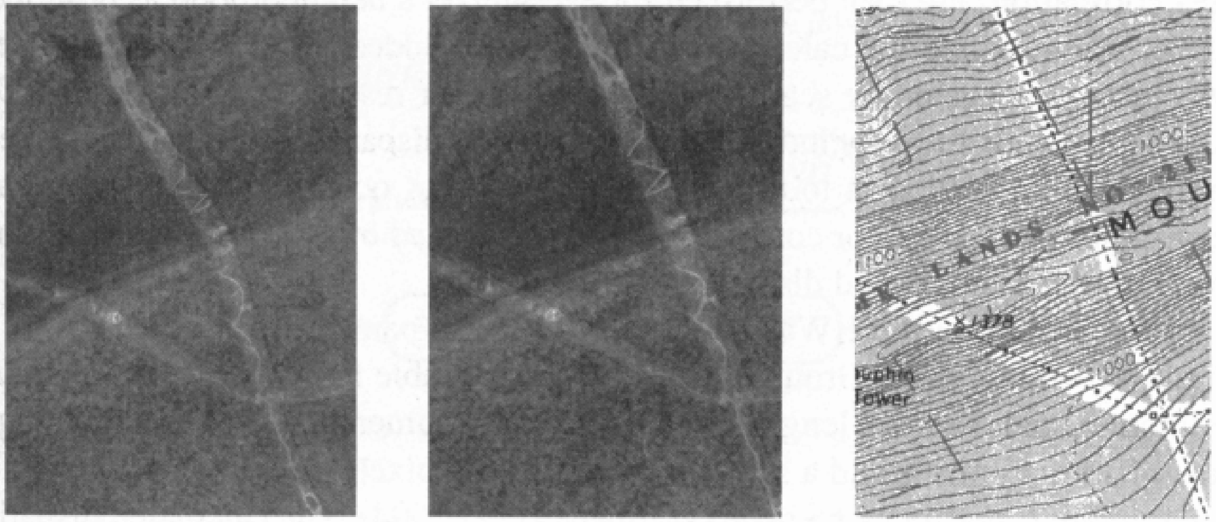

scanned photo *orthophoto* *topographic map*

FIGURE 8-8. Evidence of the orthographic projection achieved by the digital orthophoto process. The "roads" are access right-of-ways to power lines.

Polynomial geometric warps

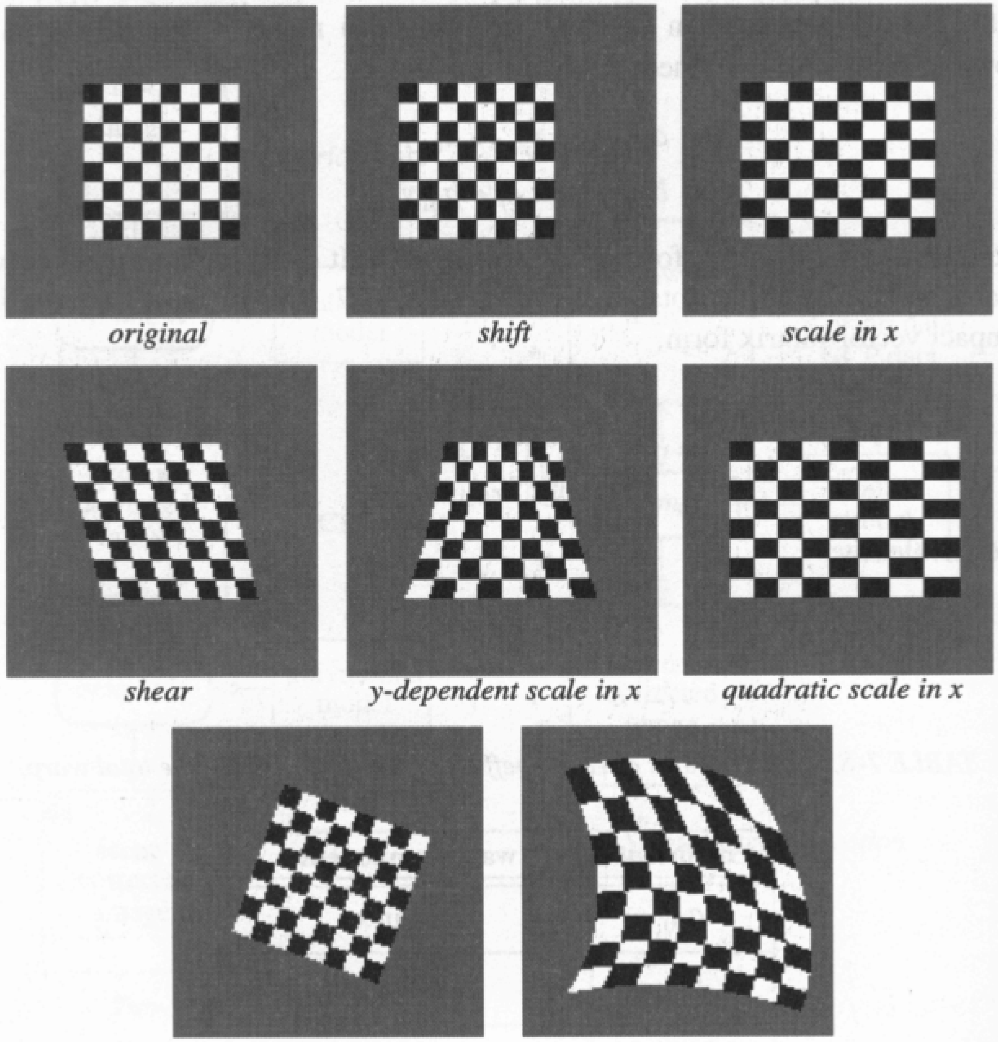

original *shift* *scale in x*

shear *y-dependent scale in x* *quadratic scale in x*

rotation *quadratic*

FIGURE 7-30. Polynomial geometric warps. The upper two rows show 1-D warps in the x-direction. Nearest-neighbor resampling is used in these examples.

$$\begin{aligned} x &= a_{00} + a_{10}x_{ref} + a_{01}y_{ref} + a_{11}x_{ref}y_{ref} + a_{20}x_{ref}^{2} + a_{02}y_{ref}^{2} \\ y &= b_{00} + b_{10}x_{ref} + b_{01}y_{ref} + b_{11}x_{ref}y_{ref} + b_{20}x_{ref}^{2} + b_{02}y_{ref}^{2} \end{aligned} \qquad (7-14)$$

line map

aerial photo

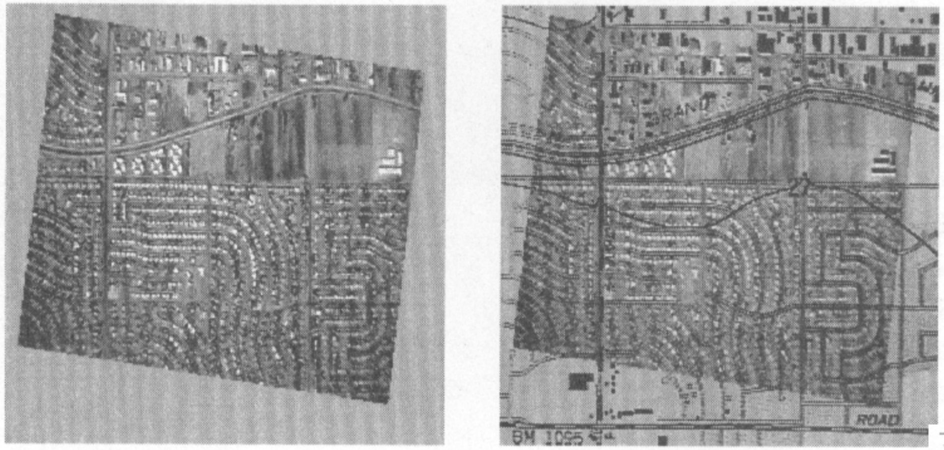

photo registered to map

composite

FIGURE 1-2. An example of how maps and imagery complement each other. The line map of an area in Phoenix, Arizona, produced manually from a stereo pair of aerial photographs and scanned into the digital raster form shown here, is an abstraction of the real world; it contains only the information that the cartographer intended to convey: an irrigation canal (the Grand Canal across the top), roads, elevation contours (the curved line through the center), and large public or commercial buildings. An aerial photograph can be registered to the map using image processing techniques and the two superimposed to see the differences. The aerial photo contains information about land use which is missing from the map. For example, an apartment complex that may not have existed (or was purposely ignored) when the map was made can be seen as a group of large white buildings to the left-center. Also, agricultural fields are apparent in the aerial photo to the right of the apartment complex, but are not indicated on the line map. In the lower half, the aerial photo shows many individual houses that also are not documented on the map.

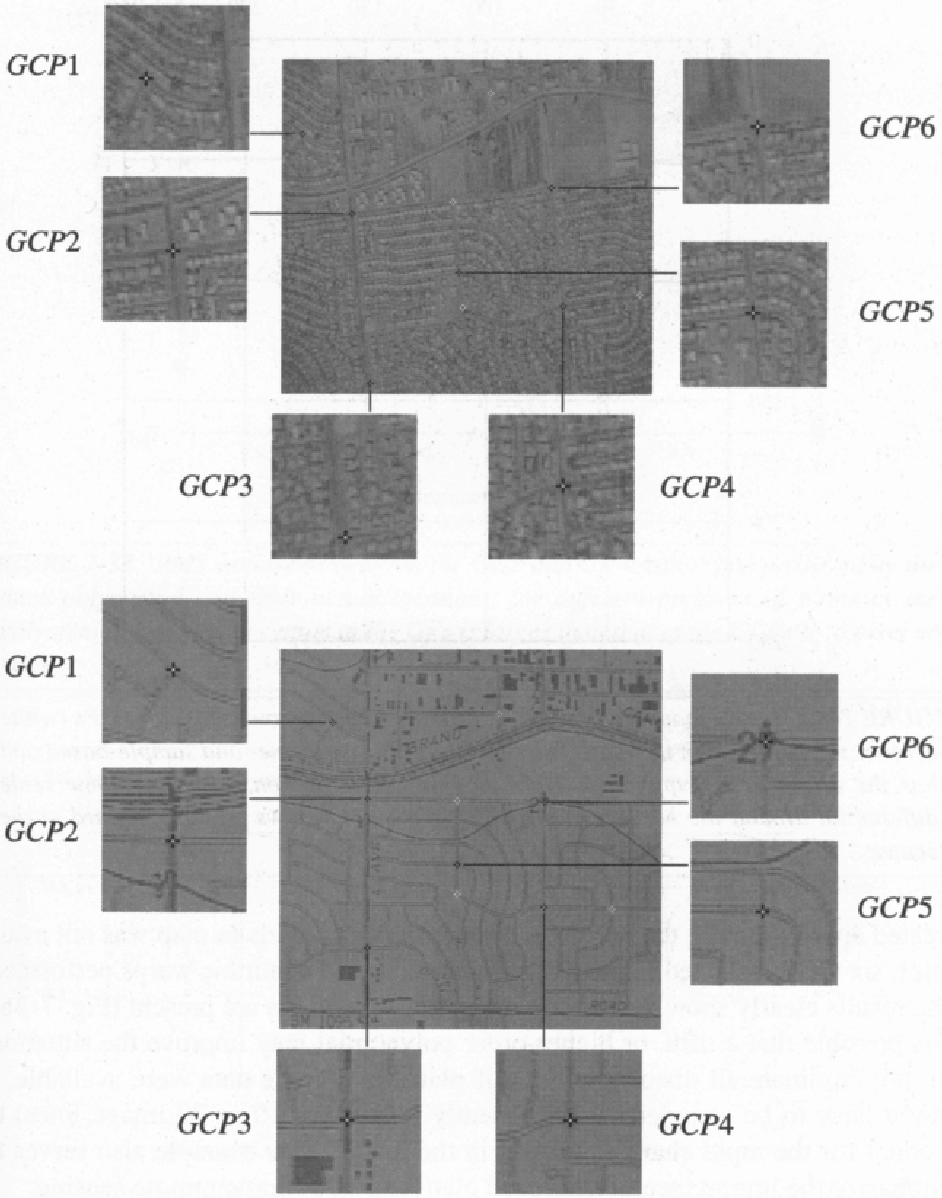

FIGURE 7-31. GCP location for rectifying the aerial photograph (top) to the scanned map (bottom). Six GCPs are selected for control (black crosses with white center) and four GPs for testing (white crosses with black center). The contrast of the image and map are purposely made low to emphasize the GCPs and GPs in this figure.

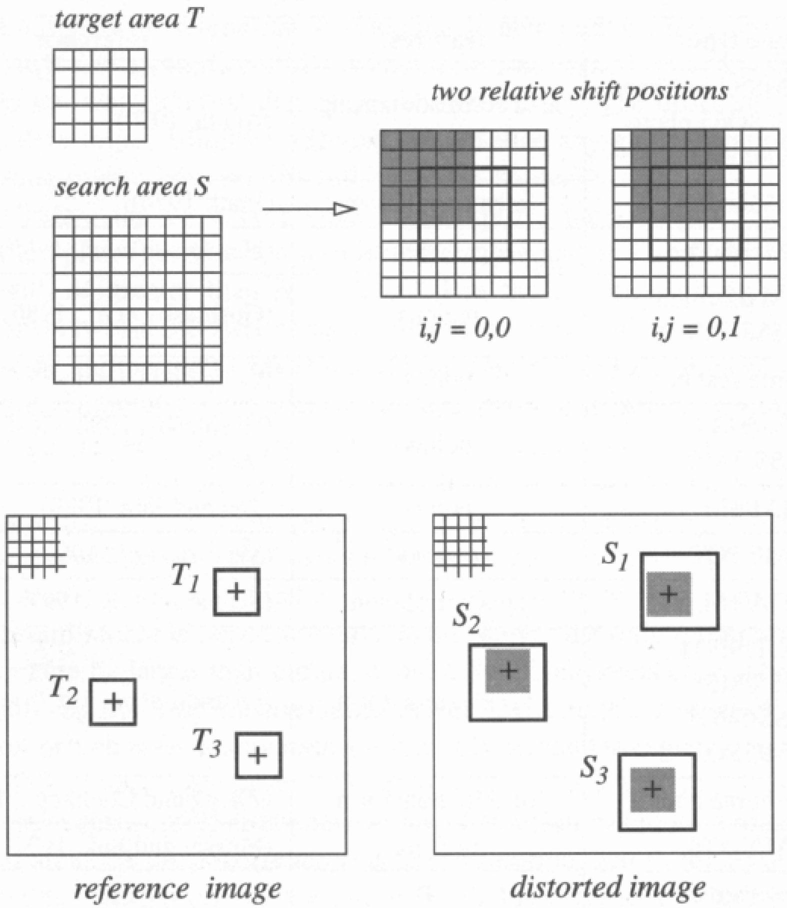

FIGURE 8-2. Area correlation for image registration. A 5 x 5 pixel target area, T, and a 9 x 9 search area, S, are shown at the top. The DN arrays are correlated by "sliding" the target patch over the search area and calculating Eq. (8 – 2) at each possible shift position (only the first two are shown; the bold square shows the L x L possible shift locations)). In this example, N and L are each five. At the bottom, we have a distorted image which is to be registered to the reference image. Three patches are used to find the distorted image coordinates at which maximum cross-correlation is obtained, possibly at fractional row and column values. The crosses in the distorted and reference images then represent the same ground point which is, in effect, a GCP. With these three GCPs, a global affine transformation can be performed.

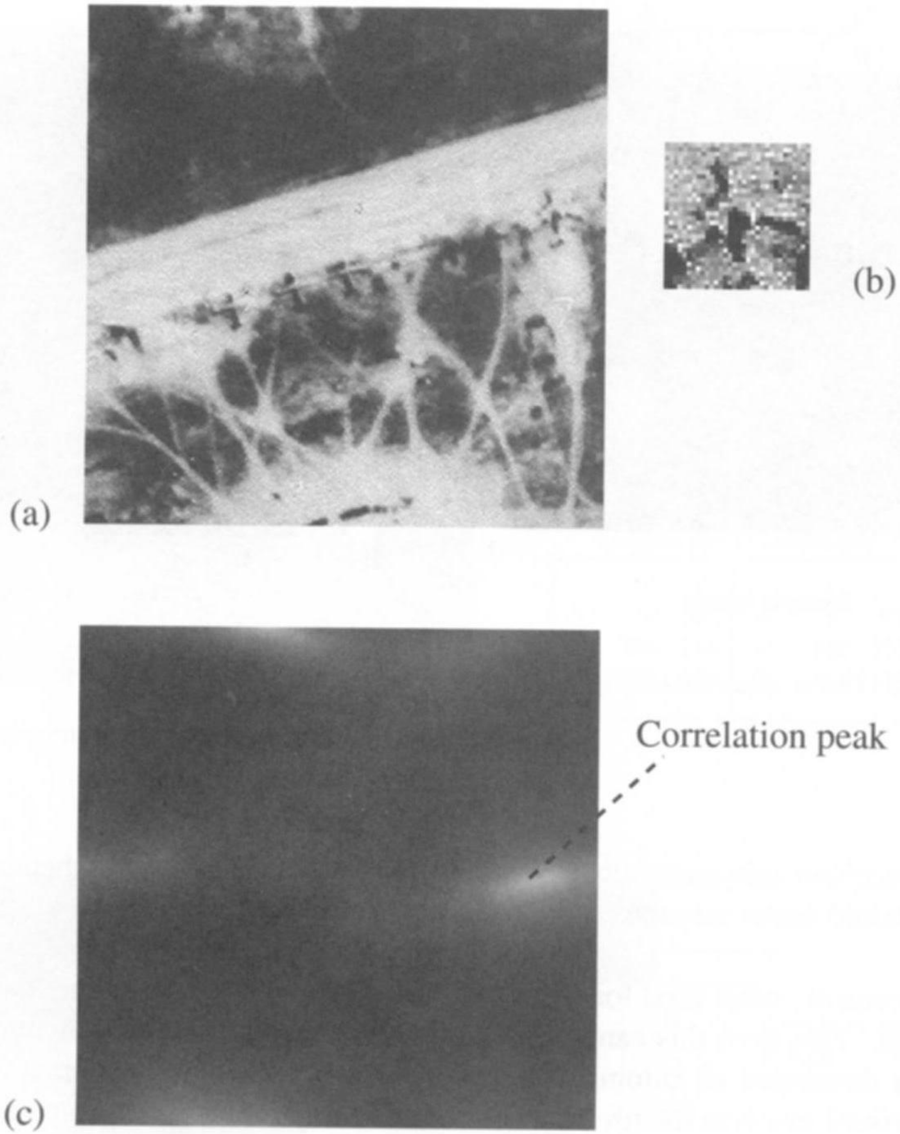

Figure 8.12 (a) Search window, (b) image kernal, and (c) correlation surface. The peek in the correlation shows where the image kernal matches the brightness structure in the search window.

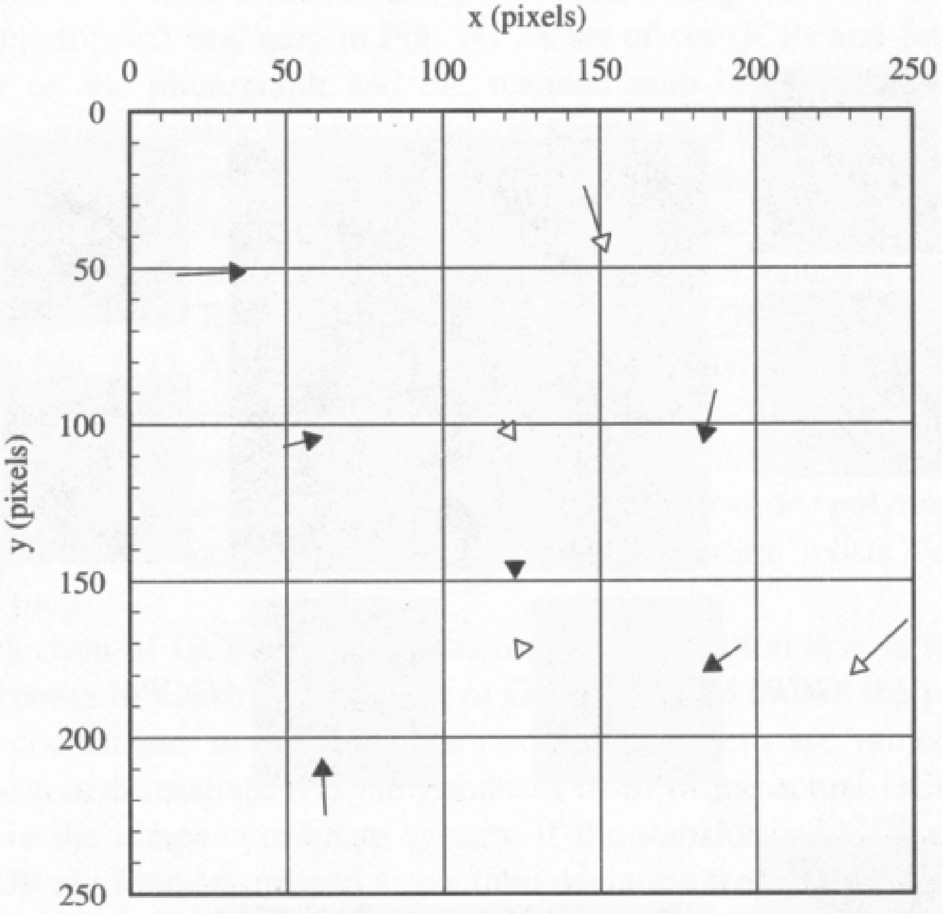

FIGURE 7-32. Direct mapping of the image GCPs (black arrowheads) and GPs (white arrowheads) to those in the map. The coordinate system is line- and sample-based and has the origin at the upper left. Note the clockwise rotation, with also some scale differential around the borders indicated by the outer arrows pointing inward to the center.

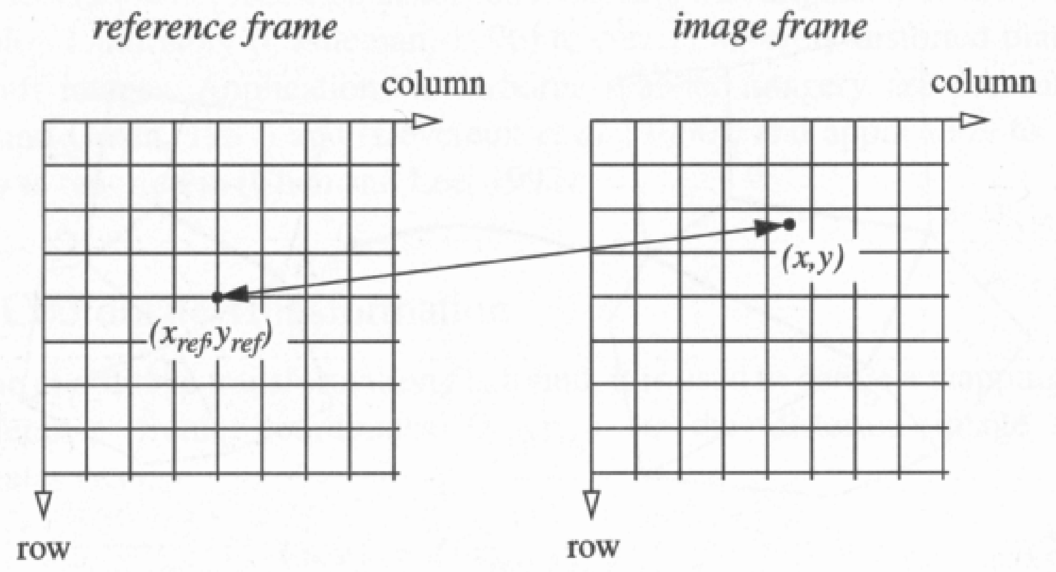

FIGURE 7-38. The two-way relationship between the reference and distorted coordinate systems, expressed as rows and columns in the digital data. The arrow from (x_{ref}, y_{ref}) to (x,y) indicates a pointer, given by Eq. (7 – 27), from an integer coordinate in the reference frame to a (generally) non-integer coordinate in the image frame. The arrow from (x,y) to (x_{ref}, y_{ref}) indicates the transfer of an estimated pixel value, resampled at the non-integer location (x,y) in the original, distorted image, to the output location (x_{ref}, y_{ref}) in the reference frame.

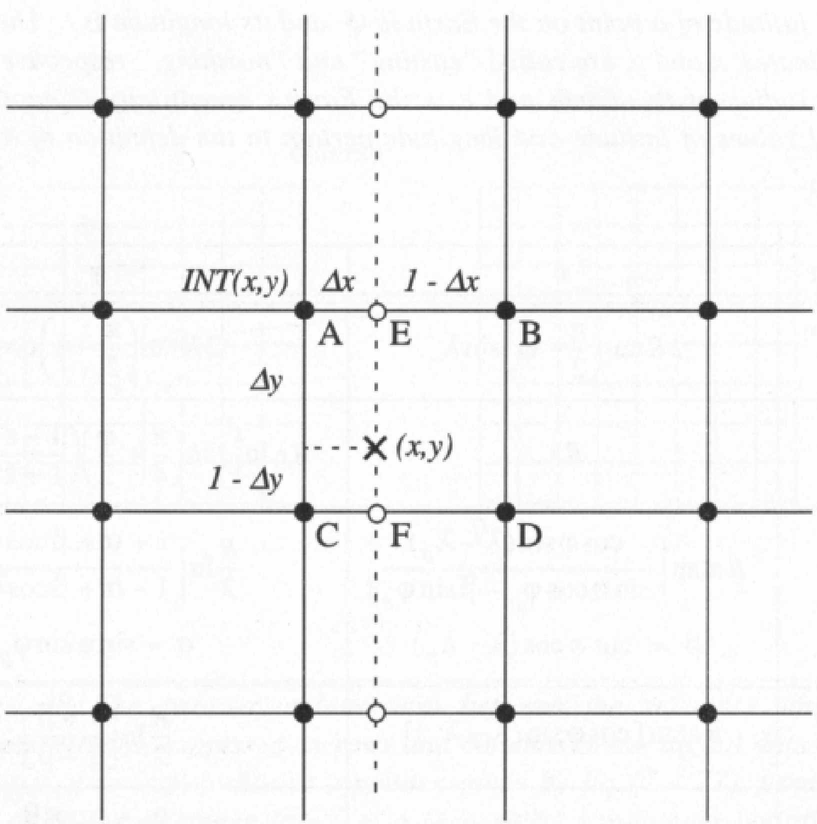

FIGURE 7-39. Geometry for resampling a new pixel at (x,y). Pixels in the distorted image (solid circles) are located at integer row and column coordinates in the image frame (Fig. 7-38). The coordinates of the local origin at pixel A are the integer parts and the offsets (Δx,Δy) are the fractional parts of (x,y) as calculated in Eq. (7 – 27). For the two-step, separable implementation of bilinear resampling, the pixels E and F are first calculated by interpolation between A and B, and C and D, respectively. Then the DN at (x,y) is estimated by interpolation between E and F. If cubic resampling is used, the four intermediate pixels (open circles) are interpolated from the surrounding four pixels in each row, and then used to estimate the DN at (x,y).

$$\begin{aligned} DN = {} & [\Delta x DN_B + (1 - \Delta x) DN_A](1 - \Delta y) \\ & + [\Delta x DN_D + (1 - \Delta x) DN_C]\Delta y \end{aligned} \quad . \qquad (7-28)$$

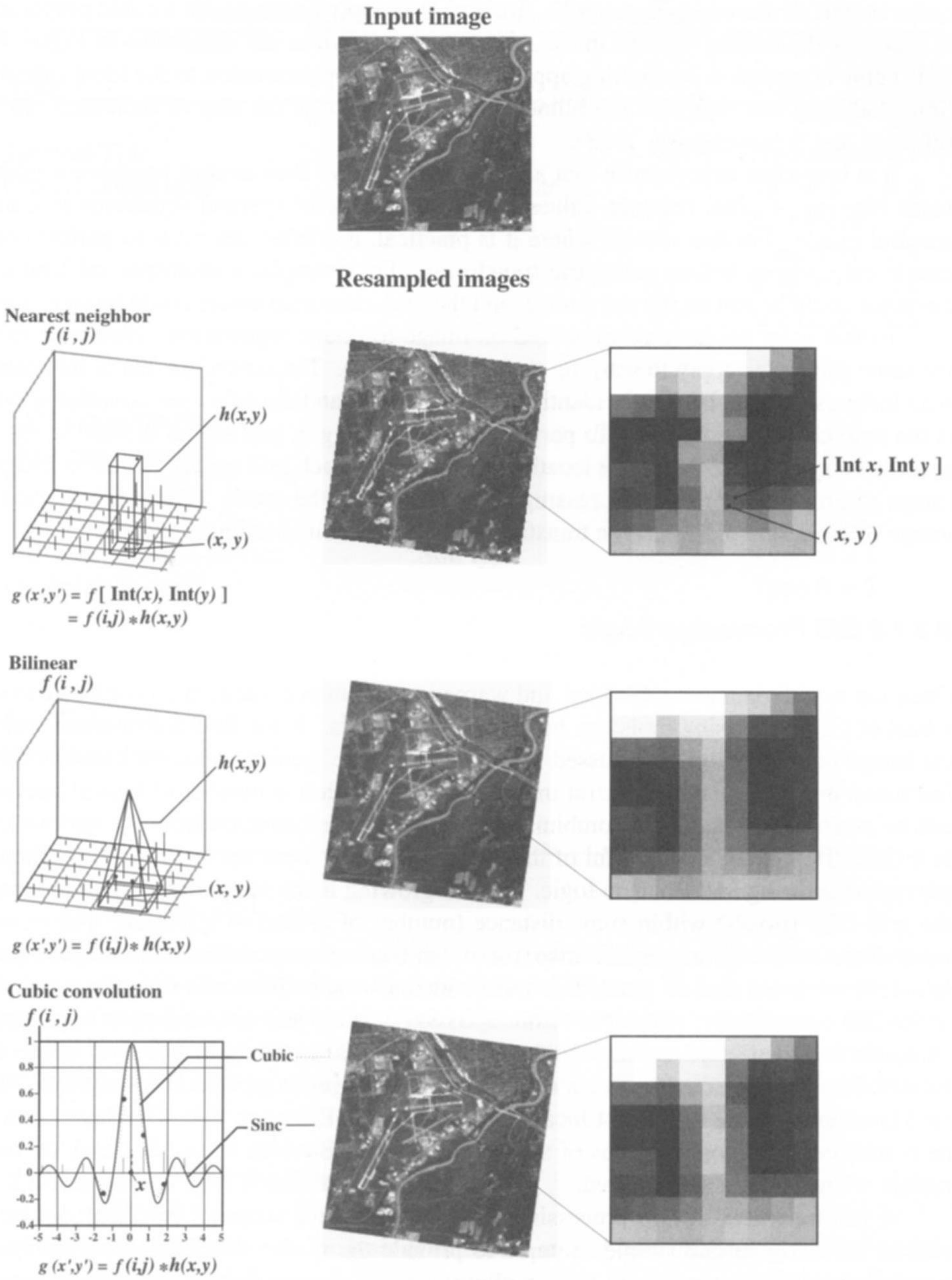

Figure 8.13 Resampling methods used in image registration.

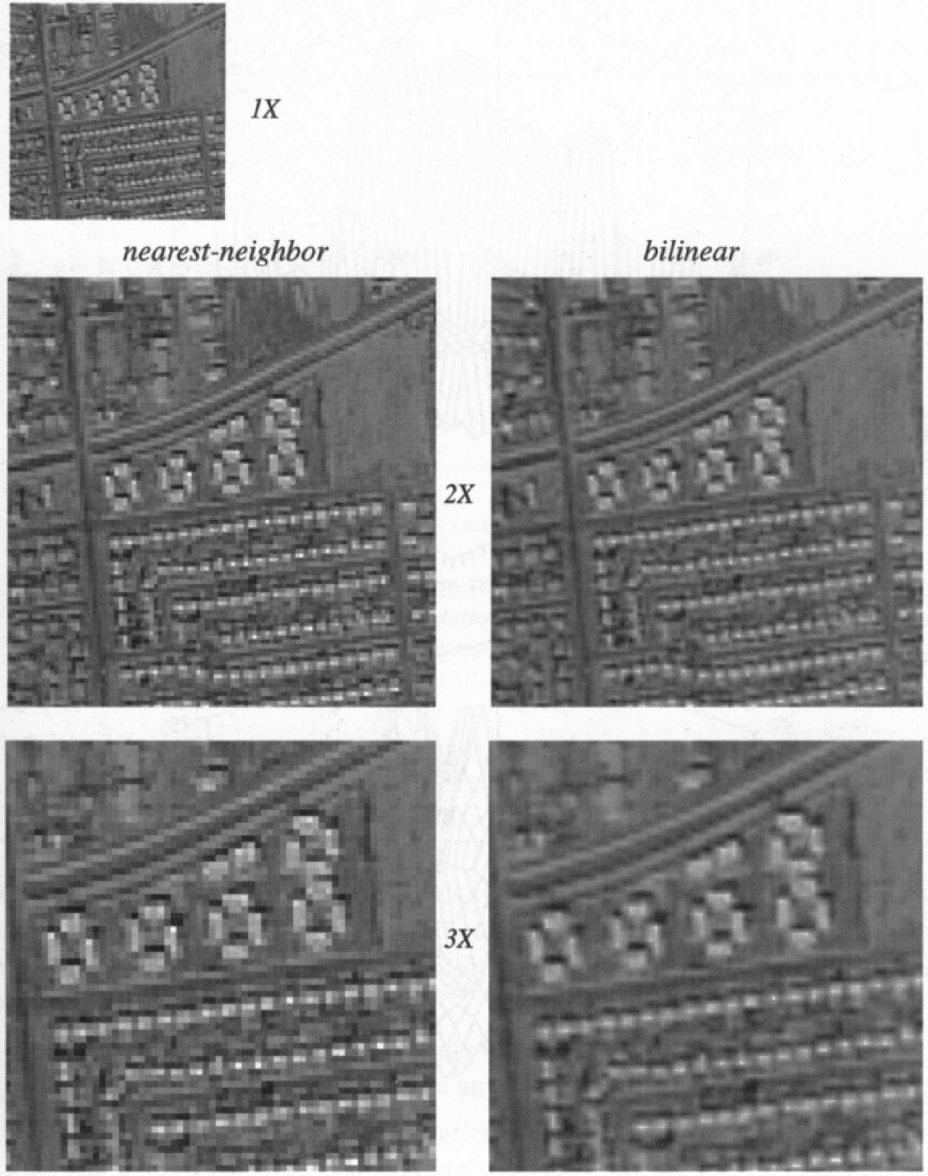

FIGURE 7-41. Image magnification using nearest-neighbor and bilinear resampling. Although the bilinear resampling is smooth, there remains a jagged "stairstep" pattern along the curved road at the top. This is aliasing that originated in the digitization of the photograph.

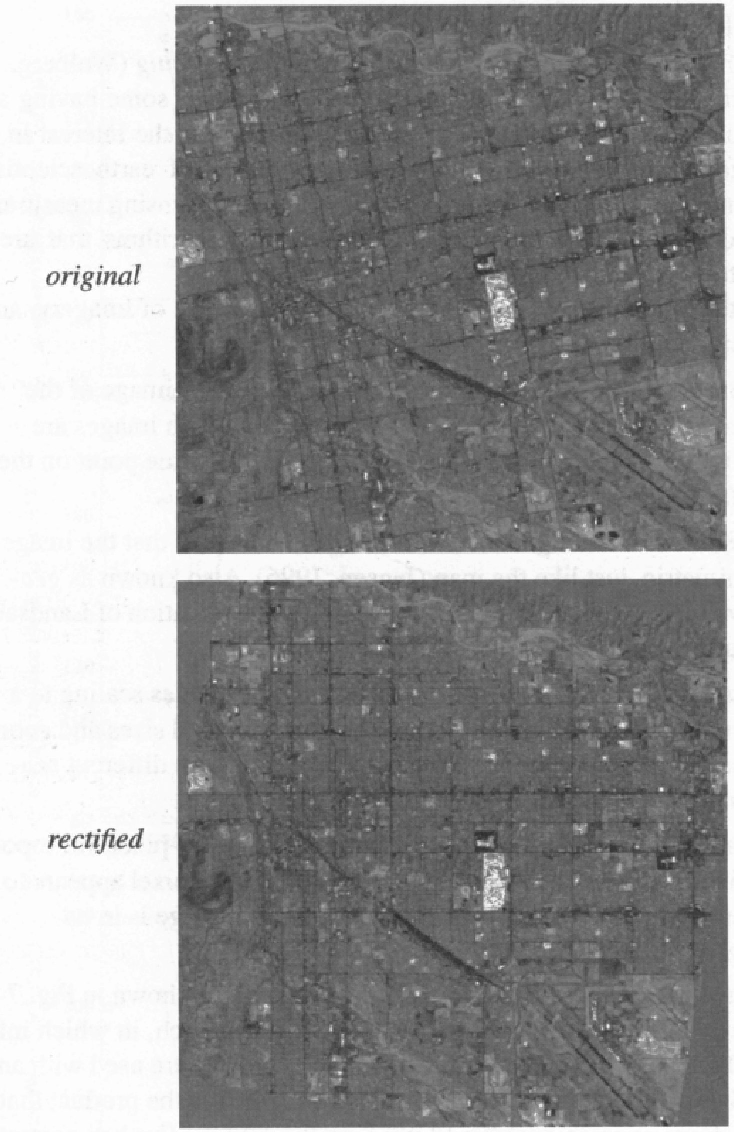

FIGURE 7-28. Rectification of a Landsat TM band 4 image of Tucson, Arizona. The primary distortion in the original is due to the non-polar orbit; thus, rotation is the dominant correction (the major streets in Tucson are oriented north and south, and east and west). Note the corners of the rectified image are clipped by the image format; a larger output format would avoid this. Also, there are some areas in the rectified frame for which no input pixels exist in the original image. These pixels are filled with a uniform DN in the output.